Ollscoil na h-Éireann, Corcaigh

An investigation of the influence of plasma parameters on the spectra of helium plasmas

A thesis submitted for the degree of
Master of Science

by
Brendan Joseph Cahill
February 2012

Academic Supervisor: **Dr. P. Mc Carthy**
Head of Department: **Prof. J. McInerney**
Department of Physics
University College Cork

CONTENTS

1. Introduction and Theoretical Background 1

1.1 Introduction 1

1.2 Plasma physics theory 2

1.2.1 Definition of a plasma 2

1.2.2 Plasma parameters 3

1.2.3 Debye shielding and the Debye length 3

1.2.4 The Plasma parameter 6

1.2.5 The plasma frequency 7

1.2.6 Collected plasma criteria 7

1.2.7 Maxwell distribution function 8

1.3 Single particle motions in prescribed E and B Fields 9

1.3.1 $E = 0, B$ fixed 9

1.3.2 $E \neq 0, B$ fixed 10

1.3.3 General force $\mathbf{F}$ 10

1.3.4 Invariance of μ 11

1.3.5 Gradient B drift 12

1.3.6 Curvature drift 14

1.3.7 Magnetic mirrors 14

1.3.8 Fluid treatment and diamagnetic drift 17

1.4 Diffusion in plasmas 18

1.4.1 Diffusion in an unmagnetised plasma 18

1.4.2 Diffusion in an magnetised plasma 20

1.4.3 Ambipolar diffusion in a magnetized plasma 22

2. Experimental apparatus . . . 24
2.1 Double plasma vessel . . . 24
2.2 Pumps . . . 24
2.3 Pressure gauges . . . 27
2.4 Magnets . . . 27
2.5 The filament and associated circuits . . . 28
2.6 The window . . . 31
2.7 The spectroscope and associated code . . . 31
2.8 The Langmuir probe . . . 33
2.8.1 Construction . . . 33

3. Sheaths and Langmuir probe theory . . . 37
3.1 Sheaths . . . 37
3.2 Langmuir probe theory and computational implementation . . . 41
3.2.1 Assumptions . . . 41
3.2.2 IV characteristics . . . 42
3.2.3 Ion current . . . 43
3.2.4 Electron current . . . 45
3.2.5 Output . . . 47

4. Results and analysis . . . 48
4.1 Examination of density and temperature along the axis of the vessel . . . 48
4.2 Pressure scans . . . 55
4.2.1 Langmuir results . . . 55
4.2.2 Spectroscopic results . . . 58
4.2.3 Investigating relationship between pressure and plasma current . . . 60
4.3 Plasma current scans . . . 61
4.3.1 Langmuir results . . . 61
4.3.2 Spectroscopic results . . . 63
4.3.3 Investigating the relationship between plasma current and filament current . . . 65

4.4 Energy scans 66
4.4.1 Langmuir results 66
4.4.2 Spectroscopic results 69
4.5 Investigating impact of the throttle thickness on fitted temperatures and densities 72
4.6 An investigation into changes in heating current 72
4.7 Investigating the magnetic confinement 75

5. Conclusion 78

6. Ideas for future research 80

7. Appendix 84
7.1 Program to analyze spectral data 84

LIST OF FIGURES

1.1 Debye shielding 4
1.2 Diagram of curvature drift 14
1.3 Loss cone in velocity space 16
1.4 Diagram of diamagnetic drift 17

2.1 Double plasma vessel 25
2.2 Rotary vane pump 25
2.3 Strength of magnetic field along axis of magnetic mirror 29
2.4 Interior of double plasma vessel showing filament 30
2.5 Sample spectrum showing background and emission peaks 32
2.6 Procedure for removing background 32
2.7 Background 33
2.8 Picture of Langmuir probe 34
2.9 Schematic of axial Langmuir probe 35
2.10 Circuit diagram of probe and Picoscope channels 36

3.1 Regions of sheath 38
3.2 a) Ideal characteristic b) Realistic characteristic 42
3.3 Ion orbits 44
3.4 The components of the ion current 45
3.5 Data with fitted model 47

4.1 The cold electron density for several pressures plotted against probe position 49
4.2 The hot electron density for several pressures plotted against probe position 49
4.3 The cold electron temperature for several pressures plotted against probe position 50

4.4 The hot electron temperature for several pressures plotted against probe position 50
4.5 The cold electron temperature for two plasma currents plotted against probe position 51
4.6 The hot electron temperature for two plasma currents plotted against probe position 51
4.7 The cold electron density for two plasma currents plotted against probe position 52
4.8 The hot electron density for two plasma currents plotted against probe position 52
4.9 The relationship between the pressure and the hot and cold densities at a filament bias voltage of 100V 56
4.10 The relationship between the pressure and the hot and cold temperatures at a filament bias voltage of 100V 56
4.11 The relationship between the pressure and the total density at a filament bias voltage of 100V 57
4.12 The relationship between the pressure and the floating potential at a filament bias voltage of 100V 57
4.13 Density and temperature with respect to pressure 58
4.14 A pressure scan at a filament bias voltage of 60V 59
4.15 A pressure scan at a filament bias voltage of 60V normalised to the plasma current 59
4.16 A pressure scan at a filament bias voltage of 70V and filament current of 13.00A showing the effect of a varying pressure on the plasma current in an unmagnetised plasma at two values of throttle thickness 60
4.17 The relationship between the plasma current, the hot and cold temperatures and the floating potential 62
4.18 The relationship between the plasma current and the hot and cold densities 62
4.19 Peak strengths plotted against plasma current for a pressure of 1 mTorr . 63

4.20 Peak strengths of 728.1 nm line for several bias voltages as the plasma current in increased. 64
4.21 Ratio of selected lines plotted against increasing plasma current 65
4.22 A scan of the filament current needed to generate a given plasma current 66
4.23 The relationship between total density and bias voltage at 1 mTorr 67
4.24 The relationship between the floating potential and bias voltage at 1 mTorr 68
4.25 The relationship between the bias voltage and the hot and cold densities at a pressure of 1 mTorr 68
4.26 The relationship between the bias voltage and the hot and cold temperatures at a pressure of 1 mTorr 69
4.27 Voltage scan at a pressure of 1 mTorr 70
4.28 Voltage scan at several pressures showing strength of 728.1 nm line 70
4.29 Ratio of selected lines plotted against bias voltage 71
4.30 Hot and cold densities plotted against inverse of throttle thickness 72
4.31 Ratio of difference in filament current to the resulting plasma current . . 73
4.32 Circuit diagram of plasma and filament circuit 74
4.33 Hot and cold densities at two bias voltages as magnet/wall separation is increased 76
4.34 Hot, cold and total densities as stack length is increased 76
4.35 Hot and cold temperatures as stack length is increased 77
4.36 Cold density plotted against pressure for all magnet diameters 77

LIST OF TABLES

2.1 Magnetic flux density at the vessel centre. 28

2.2 Engineering parameters 31

ACKNOWLEDGEMENTS

I would like to acknowledge the invaluable assistance of my supervisor, Dr. Patrick J. McCarthy, the assistance of Prof. Tom Morgan and Prof. Richard Armstrong, and the help provided by the support staff in UCC Physics Department. I wish to thank IRCSET for providing me with funding as part of the EMBARK Initiative.

ABSTRACT

The development of fusion tokamaks as a future energy source requires the ability to reliably measure the densities and temperatures present in the plasma. Spectroscopy provides a means of carrying out these measurements. This thesis investigates the spectra of helium plasmas with parameters approaching those present at the edge of a tokamak plasma. A magnetic mirror was used to confine the plasma generated by thermionic emission from a filament. Both Langmuir probe and spectroscopic results are presented. The data obtained using the Langmuir probe was fitted using a bi-Maxwellian model for the electron population; this allowed the electrons to be separated into two populations, a hot population and a cold population, with distinct temperatures and densities. The behaviour of these fitted temperature and density values was investigated as the underlying parameters of the apparatus—the bias voltage on the filament, the current passing through the filament, the neutral helium pressure and magnetic field—were varied. The cold density was shown to increase linearly with increasing bias voltage on the filament. It was also shown that the hot temperature at fixed bias voltage decreased with increasing neutral pressure.

1. INTRODUCTION AND THEORETICAL BACKGROUND

1.1 Introduction

Plasma physics was established as a subdiscipline of physics in the 1920s due to research into gas discharges and long distance communication with radio waves. The name *plasma* was suggested by one of the pioneers of the field, Irving Langmuir. Langmuir borrowed the term from physiology where it was originally coined by Purkinje, and denoted the medium in which red blood corpuscles, white blood cells and platelets moved; the word plasma derives from means "that which molds" in Greek. The use of the term is in some sense unfortunate since the analogy to a medium transporting blood cells is not an apt one; the plasma referred to by physicists is the collective name given to ionised particles, electrons and neutral atoms - the particles are the medium rather than being held in one.

The theory of Magnetohydrodynamics was developed by Hannes Alfvén during World War Two, and proved very useful in descriptions of astrophysical plasmas. The dawn of the Cold War lead to the classification of much research in the areas relating to thermonuclear fusion, the realisation that controlled fusion would not be quickly attainable and had limited military impact led to declassification in the late 50s. Several methods of plasma confinement were investigated in the postwar years, including the magnetic mirror, which forms the basis for this research. The failure to achieve long term confinement in these experiments lead to the development of the tokamak, which remains the most promising setup for achieving break-even fusion. Plasma physics research in the modern era is focused in several main areas: tokamak research and associated fusion research, astrophysical plasmas, and industrial processes in the microelectronics industry such as surface etching and deposition.

The aim of this Masters was to investigate a helium plasma generated in the Double Plasma Vessel and confined using a magnetic mirror. The investigation was performed using a Langmuir probe and a spectroscope. A Langmuir probe allows measurements of the density and temperature of the species in the plasma to be made. In this case the electon component of the plasma was modelled using a Bi-Maxwellian model consisting of two populations with differing temperatures and pressures. This produced many excellent fits to the data being modelled.

Spectroscopy enables the measurement of sprectral emission line intensities. Several ratios of lines in the helium emission spectrum are known to be temperature or density dependent and these ratios were investigated. Behaviour of line intensities with increasing pressure, plasma current and bias voltages were also investigated.

The apparatus was able to produce densities ranging from $10^9\,\mathrm{cm}^{-3}$ to $10^{10}\mathrm{cm}^{-3}$ and the temperatures of the hot populations were of the order 10eV.

1.2 Plasma physics theory

This section is based on the lecture notes of Dr. Patrick J. McCarthy and introductory textbooks by Chen[1], Goldston[5] and Bellan[3].

1.2.1 Definition of a plasma

A plasma is a quasineutral gas of charged and neutral particles which exhibit collective behaviour[1]

Consider, for example, a gas consisting of initially neutral particles in which the kinetic energy exceeds the binding energy, then on collisions there is a reasonable probability that an ionising event will occur. The three resulting populations (neutral atoms, electrons and positive ions) form a plasma.

The motion of particles in a neutral gas are dominated by collisions between particles. These collisions are an inherently short range phenomenon. Due to the charged nature of plasmas, it is immediately clear that the electric and magnetic forces will impact significantly on how the particles move. Both of these forces are long range in nature.

If long range forces dominate the short range collisional effects, the plasma is called *collisionless*. Collisions simplify the analysis of plasma behaviour because they drive the system towards equilibrium values.

Quasineutrality implies that if all the ions are carrying a single charge:

$$n_i \simeq n_e \tag{1.2.1}$$

where n_i is the ion density and n_e the electron density.

1.2.2 Plasma parameters

The basic parameters which define a plasma are

- the particle density n,
- the temperature T of each species,
- the magnetic field B.

For this thesis, the temperature will always be given in eV unless otherwise stated. The conversion from eV to K just involves multiplying by e/k_B where e is the electron charge and k_B is Boltzmann's constant. The densities are quoted in particles per cm^{-3} and the magnetic fields are quoted in Tesla or milliTesla as appropriate.

1.2.3 Debye shielding and the Debye length

Consider an initially spatially uniform plasma formed from a statistically large number of ions and electrons whose number densities are equal. The two populations are allowed to have different temperatures: T_i and T_e.

Thermal motion of the two populations will lead to local perturbations in the relative abundances of two species, which, in turn, results in the establishment of electrostatic potentials, ϕ, in the plasma.

Like charges repel, and since the charges in plasma are mobile, this leads to a screening effect around any electrical potential, which is referred to as *Debye shielding*.

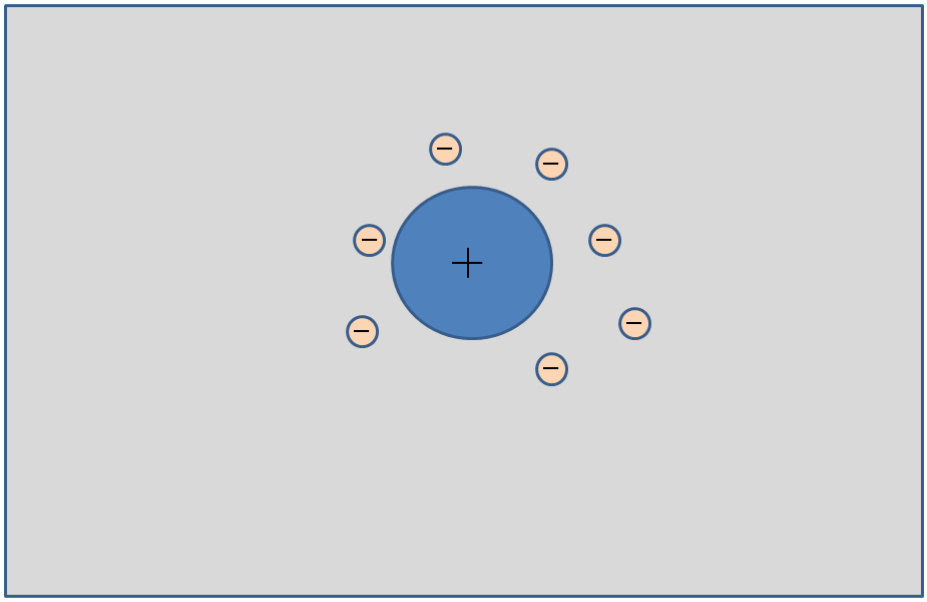

Fig. 1.1: Debye shielding

To understand how the effect works, imagine slowly introducing a test charge Q to an initially spatially homogeneous, neutral, collisionless plasma [3], and examine how this will effect the local electrical potential.

First consider each species in the plasma as a fluid obeying a collisionless equation of motion given by:

$$m_s \frac{d\mathbf{u}_s}{dt} = q_s \mathbf{E} - \frac{1}{n_s} \boldsymbol{\nabla} P_s, \tag{1.2.2}$$

where s denotes the species in question, P is the pressure, $\mathbf{E}$ is the electric field strength, q is the charge on a particle and $\mathbf{u}$ is the velocity of a particle.

The first term on the right hand side can be assumed to be electrostatic in nature, and therefore $\mathbf{E} \sim \nabla\phi$. The left hand side of the equation may be ignored in the common case where the inertial contribution to the motion is negligible. If we assume that each species has a uniform temperature in both space and time, i.e. that gradients in space are removed by thermal motions and that any perturbation which occurs does not remove the plasma from thermal equilibrium, we can write that $P_s = n_s k_B T_s$. These

approximations allow the above equation to be rewritten as

$$0 \approx n_s q_s \nabla\phi - k_B T_s \nabla n_s. \tag{1.2.3}$$

This results in the *Boltzmann relation*

$$n_s = n_{s0} \exp(-\frac{q_s \phi}{k_B T_s}). \tag{1.2.4}$$

Now, to study the impact of the test charge on the surrounding plasma, *Poisson's equation* must be used

$$\nabla^2 \phi = -\frac{1}{\varepsilon_0} \left[Q\delta(\mathbf{r}) + \sum_s n_s(\mathbf{r}) q_s \right], \tag{1.2.5}$$

where the first term refers to the test charge and the second term gives the contribution from the perturbed background charges to the potential. Using Eq. (1.2.4) and assuming that $q_s\phi \ll k_B T_s$, Eq. (1.2.5) becomes:

$$\nabla^2 \phi = -\frac{1}{\varepsilon_0} \left[Q\delta(\mathbf{r}) + \left(1 - \frac{q_e\phi}{k_B T_e}\right) n_e q_e + \left(1 - \frac{q_i\phi}{k_B T_i}\right) n_i q_i \right] \tag{1.2.6}$$

Using the earlier assumption that the initial plasma was neutral, this can be simplified further:

$$\nabla^2 \phi - \frac{1}{\lambda_D^2}\phi = -\frac{Q}{\varepsilon_0}\delta(\mathbf{r}), \tag{1.2.7}$$

where the λ_D is called the effective *Debye length*, which is composed of the two species' Debye lengths:

$$\frac{1}{\lambda_D^2} = \sum_s \frac{1}{\lambda_s^2}. \tag{1.2.8}$$

The Debye length for each species is given as follows:

$$\lambda_s^2 = \frac{\varepsilon_0 k_B T_s}{n_{s0} q_s}. \tag{1.2.9}$$

Solving Poisson's equation gives:

$$\phi(\mathbf{r}) = \frac{Q}{4\pi\varepsilon_0 r} e^{-r/\lambda_D}, \tag{1.2.10}$$

which is a *Yukawa potential*. For small r, i.e. $r \ll \lambda_D$, the solution converges to that of a isolated charge in a vacuum, but for $r \gg \lambda_D$, the charges in the plasma will screen out the test charge.

Clearly the degree of screening decreases as the density decreases and their are fewer particles available in a given area also as the temperature rises the ability to screen out charges diminishes, this is because a growing fraction of electrons will be too energetic to remain bound in the electric field around the positive charge.

1.2.4 The Plasma parameter

The *plasma parameter* is defined as the number of particles in a *Debye sphere*; a sphere whose radius is the Debye length:

$$\Lambda = n\frac{4\pi}{3}\lambda_D^3. \tag{1.2.11}$$

substituting for λ_D gives:

$$\Lambda = \frac{1}{\sqrt{n}}\frac{4\pi}{3}\left(\sqrt{\frac{\varepsilon_0 T}{e^2}}\right)^3. \tag{1.2.12}$$

Defining the average distance between particles as:

$$r_d \equiv n^{-1/3}, \tag{1.2.13}$$

and the distance of closest approach, r_c, as the distance at which the kinetic energy of the particle is fully converted to potential energy,

$$r_c \equiv \frac{e^2}{4\pi\varepsilon_0 T}, \tag{1.2.14}$$

allows us to rewrite the plasma parameter as follows:

$$\Lambda = \frac{1}{6\sqrt{\pi}}\left(\frac{r_d}{r_c}\right)^{3/2}. \tag{1.2.15}$$

The significance of this result is that when $\Lambda \ll 1$, the particles in the plasma are dominated by one another's electrical fields and are called *strongly coupled*. If the Debye sphere is densely populated, $\Lambda \gg 1$, the particle only experiences the electrical influences of particles within its Debye sphere. Such a plasma is called *weakly coupled*.

1.2.5 The plasma frequency

If we displace the electrons in a plasma by a distance, δx, from their initial position against a background of uniform positive ions, which we treat as remaining fixed, the electrons will oscillate about their original position due to their inertia causing them to overshoot their initial position as the electric field returns them to equilibrium. The resulting oscillations are simple harmonic in nature, governed by:

$$m\frac{d^2\delta x}{dx^2} = -e\frac{en}{\epsilon_0}\delta x. \tag{1.2.16}$$

A frequency called the *plasma frequency* can be attributed to the motion, and is defined as follows:

$$\omega_p = \sqrt{\frac{ne^2}{\varepsilon_0 m_e}}. \tag{1.2.17}$$

Above ω_p, electromagnetic waves can propagate through the plasma, but below the plasma frequency, the electrons move to screen out the disturbance. The plasma frequency also suggests a characteristic time, τ_p, over which disturbances may be observed.

1.2.6 Collected plasma criteria

So, in summary, to qualify as a plasma, the collection of charged and uncharged particles must conform to the following properties:

$$\lambda_D \ll L, \tag{1.2.18}$$

$$\Lambda \gg 1, \tag{1.2.19}$$

$$\omega_p \tau > 1, \tag{1.2.20}$$

where L and τ are, respectively, the characteristic length scale and time scale of the process being investigated.

1.2.7 Maxwell distribution function

The distribution of particle velocities for a gas in thermal equilibrium is given by the Maxwell distribution:

$$f(u) = A \exp\left(\frac{-\frac{1}{2}mu^2}{kT}\right). \tag{1.2.21}$$

From this, the density of particles and average energy can be computed by integration over all possible velocities:

$$n = \int_{-\infty}^{\infty} f(u)du, \tag{1.2.22}$$

and

$$E_{av} = \frac{\int_{-\infty}^{\infty} \frac{1}{2}mu^2 f(u)du}{\int_{-\infty}^{\infty} f(u)du}. \tag{1.2.23}$$

In three dimensions, it follows that:

$$E_{av} = \frac{3}{2}kT \tag{1.2.24}$$

Where E_{av} denotes the average kinetic energy of a particle.

It should be noted that each species in the plasma may have a different temperature i.e. T_i and T_e, the ion temperature and electron temperature, may differ due to different collision rates. The components along and perpendicular to the **B** field may have different temperatures as well.

1.3 Single particle motions in prescribed E and B Fields

1.3.1 $E = 0, B$ fixed

In the absence of an electric field, a charged particle in a constant magnetic field in the $\hat{\mathbf{z}}$ direction will obey the following equation of motion :

$$m\frac{d\mathbf{v}}{dt} = q\mathbf{v} \times \mathbf{B}. \tag{1.3.1}$$

This results in the following equation for v_x and v_y:

$$\frac{d^2 v_{x,y}}{dt^2} = -\left(\frac{qB}{m}\right)^2 v_{x,y}. \tag{1.3.2}$$

This gives rise to cyclotron gyrations at the *cyclotron frequency*:

$$\omega_c = \frac{qB}{m}. \tag{1.3.3}$$

The solutions to Eq. (1.3.2) are clearly of the form:

$$v_x = v_\perp exp(i\omega_c t + i\delta), \tag{1.3.4}$$

$$v_y = \pm i v_\perp exp(i\omega_c t + i\delta), \tag{1.3.5}$$

$$v_z = v_{zi}, \tag{1.3.6}$$

where v_{zi} is the $\hat{\mathbf{z}}$ component of the velocity, and the amplitude of the varying velocities in the plane perpendicular to the magnetic fields is denoted by $v_\perp$. This allows us to define the *Larmor radius*, r_L, as follows:

$$r_L \equiv \frac{v_\perp}{\omega_c}. \tag{1.3.7}$$

This can be expressed in terms of fundamental parameters using the expression for ω_c above:

$$r_L \equiv \frac{m v_\perp}{qB}. \tag{1.3.8}$$

1.3.2 $E \neq 0, B$ fixed

Taking an arbitrary **E** and defining the axes so that $E_y = 0$ allows the motion of a particle to be described in terms of two separate components; the Larmor gyration due to the uniform **B** field and a drift of the guiding centre. The equations of motion become:

$$\frac{dv_x}{dt} = \frac{qE_x}{m} \pm \omega_c v_y, \tag{1.3.9}$$

$$\frac{dv_y}{dt} = 0 \mp \omega_c v_x, \tag{1.3.10}$$

$$\frac{dv_z}{dt} = \frac{qE_z}{m}. \tag{1.3.11}$$

Clearly the motion along **B** is easily solved for by integration:

$$v_z = \frac{qE_z}{m}t + constant. \tag{1.3.12}$$

Also

$$v_x = v_\perp \exp^{i\omega_c t}, \tag{1.3.13}$$

and

$$v_y = iv_\perp \exp^{i\omega_c t} - \frac{E_x}{B} \tag{1.3.14}$$

So, overall the type of motion remains oscillatory, but with the extra $\frac{E_x}{B}$ term. The centre of the circular path traced out by a particle, the guiding centre, is displaced linearly in time. The magnitude of the guiding centre velocity is independent of the properties of the particle; it depends only on the magnitude of the E and B fields.

1.3.3 General force **F**

If we consider a general force, **F**, at an arbitrary angle to the **B** field, then the drift velocity component parallel to **B** is given by $\dot{v}_\parallel = F/m$ and the drift velocity across the **B** field is given by:

$$\mathbf{v_d} = \frac{F_\perp}{qB} = \frac{\mathbf{F} \times \mathbf{B}}{qB^2}, \tag{1.3.15}$$

where

$$F_{\perp} = \mathbf{F} \times \hat{\mathbf{z}} = \frac{\mathbf{F} \times \mathbf{B}}{B}. \tag{1.3.16}$$

In the case of electric fields, $\mathbf{E}$, Eq. (1.3.15) becomes:

$$\mathbf{v_E} = \frac{\mathbf{E} \times \mathbf{B}}{B^2}, \tag{1.3.17}$$

which is called the $\mathbf{E} \times \mathbf{B}$ drift.

1.3.4 Invariance of μ

The magnetic moment μ is given by the product of the current flowing through a loop and the area of the loop:

$$\mu = I\pi r_L^2. \tag{1.3.18}$$

The current and Larmor radius can be substituted for giving:

$$\mu = \frac{q\omega_c}{2\pi}\pi\frac{v_{\perp}^2}{\omega_c^2} = \frac{mv_{\perp}^2}{2B}. \tag{1.3.19}$$

The magnetic potential energy is give by[1]:

$$U = -\boldsymbol{\mu}.\mathbf{B} \tag{1.3.20}$$

and

$$\mathbf{F} = -\boldsymbol{\nabla}U, \tag{1.3.21}$$

therefore the force can be rewritten in terms of $\mathbf{B}$ as follows:

$$\mathbf{F} = \boldsymbol{\nabla}(\boldsymbol{\mu}.\mathbf{B}). \tag{1.3.22}$$

In the case where $\mathbf{B}$ has a gradient parallel to $\mathbf{B}$, there is no drift perpendicular to $\mathbf{B}$ because clearly $\mathbf{F} \times \mathbf{B} = \mathbf{0}$

Due to the changing size of | **B** |, the frequency of gyration, ω_c, will change. By equation Eq. (1.3.8), the change in frequency will lead to a change in the Larmor radius and/or a change in the perpendicular velocity.

Both the energy and angular momentum of the gyrating charge will be conserved, which means that:

$$\frac{d}{dt}\left(\frac{1}{2}mv^2\right) = \frac{d}{dt}\left(\frac{1}{2}m(v_\parallel^2 + v_\perp^2)\right) = 0 \tag{1.3.23}$$

and

$$\frac{d}{dt}\left(mv_\perp r_L\right) = 0. \tag{1.3.24}$$

Substituting the expression for r_L from Eq. (1.3.7) into Eq. (1.3.24) gives:

$$\frac{d}{dt}\left(mv_\perp \frac{mv_\perp}{qB}\right) = \frac{2m}{q}\frac{d}{dt}\left(\frac{mv_\perp^2}{2B}\right) = 0. \tag{1.3.25}$$

Now using the expression for μ in Eq. (1.3.19) gives

$$\frac{d\mu}{dt} = 0. \tag{1.3.26}$$

This result also holds in the more important case of slowly varying magnetic fields.

1.3.5 Gradient B drift

In non-uniform **B** fields the ratio of the Larmor radius, r_L to the gradient scale length, L, is the most used parameter for characterising the resulting particle motions. Consider a **B** field acting in the $\hat{\mathbf{z}}$ direction which has a gradient in the $\hat{\mathbf{y}}$ direction - the $\frac{\partial}{\partial x}$ and $\frac{\partial}{\partial z}$ terms will both vanish.

B can be written as follows:

$$\mathbf{B}(x, y, z)) = (B_{gc} + (y - y_{gc})\frac{dB}{dy})\hat{\mathbf{z}}, \tag{1.3.27}$$

where y_{gc} and B_{gc} are the initial values of the the position of the guiding centre, and the value of the magnetic field at this point, respectively.

Clearly the expansion above is valid if

$$\frac{r_L}{L} \ll 1. \tag{1.3.28}$$

This implies that the scale of the gyroradius is much shorter than the scale on which the **B** field is changing.

Using

$$\mathbf{F}_{\nabla_\perp B} = -\boldsymbol{\mu}.\boldsymbol{\nabla}_\perp B\hat{\mathbf{z}}, \tag{1.3.29}$$

where

$$\boldsymbol{\nabla}_\perp B = \frac{\partial B}{\partial x}, \frac{\partial B}{\partial y} \tag{1.3.30}$$

by substituting this into Eq. (1.3.15) allows the transverse drift to be written as

$$\mathbf{v}_{\nabla_\perp B} = \frac{\boldsymbol{\mu}.\mathbf{B} \times \nabla_\perp B}{qB^2}. \tag{1.3.31}$$

This transverse drift term, which arises from the gradient in the magnetic flux density is called the *Grad B drift*.

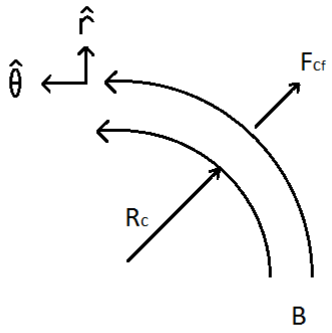

Fig. 1.2: Diagram of curvature drift

1.3.6 Curvature drift

When the field lines are curved with a radius of curvature $\mathbf{R}_c$ the particles moving in the field will experience a guiding centre drift due to centrifugal forces. The centrifugal force is given by

$$\mathbf{F_{cf}} = m\frac{v_\parallel^2}{R_c}\hat{\mathbf{r}}. \tag{1.3.32}$$

Using Eq. (1.3.15) gives the drift due to curved magnetic field lines as:

$$\mathbf{v}_R = \frac{mv_\parallel^2}{qB^2}\frac{\mathbf{R}_c \times \mathbf{B}}{R_c^2}. \tag{1.3.33}$$

1.3.7 Magnetic mirrors

Early attempts at controlled nuclear fusion attempted to utilize a confinement scheme called a *magnetic mirror* to achieve suitable densities. In a magnetic mirror the gradient is parallel to the **B** field. The total kinetic energy of particles in this technique is conserved, allowing the velocity parallel to the field to change sign and hence the particles to reverse direction, confining them within a region. The parameters affecting the motion are categorised in direction perpendicular ($\perp$), and parallel ($\parallel$) to the field.

The total kinetic energy can be broken up as follows:

$$W = W_\perp + W_\parallel. \tag{1.3.34}$$

Now

$$W_{\parallel} = \frac{mv_{\parallel}^2}{2}, \tag{1.3.35}$$

and

$$W_{\perp} = \frac{mv_{\perp}^2}{2} = \mu B. \tag{1.3.36}$$

This means that:

$$W = \frac{mv_{\parallel}^2}{2} + \mu B. \tag{1.3.37}$$

The region of weakest B in a mirror confinement apparatus, like the double plasma vessel, will be at the vessel centre. The strongest field will be just inside the vessel walls at the point where the magnets are positioned.

Clearly, when B increases, $v_{\parallel}$ must decrease to keep W, the total kinetic energy, constant. When B is sufficiently large the velocity along the field will become 0 and the particle will be reflected along its path - this is the mirror effect. The points at which this happens are called the *mirror points* or *bounce points*.

The downside to this method of confinement is that only a certain range of velocities are confined; particles which breach this critical velocity will escape the trap. The behaviour of the particles in regions of maximum magnetic field will be determined by their velocities at the mirror centre, where the field strength is weakest. Writing $W_{\perp}$ as

$$W_{\perp}(mid) = \mu B_{min} = W\frac{B_{min}}{B_{max}}, \tag{1.3.38}$$

where $W_{\perp}(mid)$ denotes the perpendicular component of the kinetic energy at the vessel centre, B_{min} is the magnetic flux density at the vessel centre and B_{max} is the magnetic flux density at the mirror points .

The overall kinetic energy at the centre of the mirror, $W(mid)$, can be written as

$$W = W_{\parallel} + W\frac{B_{min}}{B_{max}}, \tag{1.3.39}$$

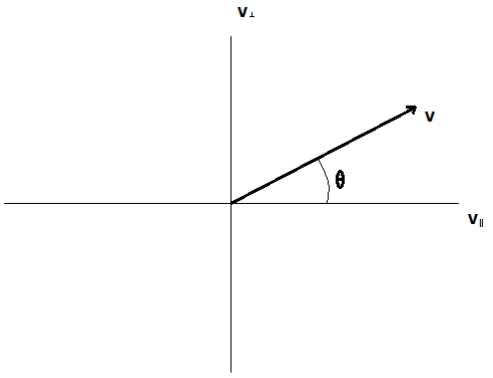

Fig. 1.3: Loss cone in velocity space

and using Eq. (1.3.35) and the formula for total kinetic energy of a particle of mass, m, and velocity, v, gives:

$$\frac{W_{\parallel}}{W} = \frac{v_{\parallel}^2}{v^2} = 1 - \frac{B_{min}}{B_{max}}. \tag{1.3.40}$$

Particles which have a velocity parallel to the field greater than given by Eq. (1.3.40)will escape the trap. The key ratio of field strengths is called the *mirror ratio*, R_m:

$$R_m = \frac{B_{max}}{B_{min}}. \tag{1.3.41}$$

Clearly as the mirror ratio increases the range of velocities falling within the loss cone decrease. Diffusion in velocity space will cause continuous losses via this route.

The range of velocities which are lost can be expressed as an angle in velocity space as shown in Fig. (1.3). The condition for electrons to remain trapped can be rewritten as:

$$\sin\theta^2 \equiv \frac{v_{\perp}^2}{v^2} \geq \frac{B_{min}}{B_{max}} \equiv \frac{1}{R_m}. \tag{1.3.42}$$

The angle at the mirror centre, θ, is called the pitch angle. Particles which have $\theta < \theta_{min}$ at the vessel centre, where $theta_{min}$ is the critical value of the pitch angle, will exit the mirror.

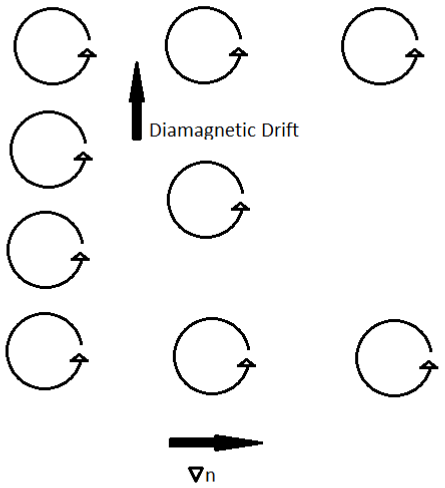

Fig. 1.4: Diagram of diamagnetic drift

1.3.8 Fluid treatment and diamagnetic drift

The equation of motion for each species is given by

$$mn\left[\frac{\partial \mathbf{u}}{\partial t} + (\mathbf{u}.\nabla)\mathbf{u}\right] = qn(\mathbf{E} + \mathbf{u} \times \mathbf{B}) - \boldsymbol{\nabla} p. \tag{1.3.43}$$

Taking a cross product of Eq. (1.3.43) and $\mathbf{B}$ gives[1]:

$$0 = qn[\mathbf{E} \times \mathbf{B} + \mathbf{B}(\mathbf{v}_\perp.\mathbf{B}) - \mathbf{v}_\perp(\mathbf{B}.\mathbf{B})] - \boldsymbol{\nabla} p \times \mathbf{B}, \tag{1.3.44}$$

where the time term on the left hand side has been neglected because we are considering drifts with slower time scales, the general velocity $\mathbf{u}$ is replaced with the motion in the perpendicular direction $\mathbf{v}_\perp$, and the $(\mathbf{v}.\boldsymbol{\nabla})\mathbf{v}$ term can be neglected since the gradient is perpendicular to the resulting drifts.

By rearranging Eq. (1.3.44) in terms of $\mathbf{v}_\perp$ the following expression is found:

$$\mathbf{v}_\perp = \frac{\mathbf{E} \times \mathbf{B}}{B^2} + \frac{-\boldsymbol{\nabla} p \times \mathbf{B}}{qnB^2} \tag{1.3.45}$$

The last term in Eq. (1.3.45) is called the *diamagnetic drift*.

This drift can be easily understood by considering a small volume containing gyrating ions with a pressure gradient perpendicular to the magnetic field. Due to the

density gradient there will be more downward motions than upward motions in a given area,(Fig. 1.4), and this results in a drift perpendicular to both the gradient and the magnetic field.

1.4 Diffusion in plasmas

The effect of collisions between particles in the plasma is to randomise the motion of the particles. In the presence of a concentration gradient, this random walk motion gives rise to diffusion of particles down the concentration gradient. The flux of particles is given by Fick's Law:

$$\Gamma = -D\nabla n. \tag{1.4.1}$$

The stepsize in question depends on whether or not the plasma is magnetized. In a magnetized plasma, the natural choice of step size between 90^o collisions is the Larmor radius, whereas in an unmagnetized plasma there are no Larmor orbits, so the mean free path between collisions is the best choice.

1.4.1 Diffusion in an unmagnetised plasma

Using $\lambda_{mfp} = v_{th}\tau$, where τ is the average time between 90^o collisions, it is possible to write the diffusion coefficient for electrons in an unmagnetized plasma as:

$$D_e = \frac{\lambda_{mfp}}{\tau} = v_{th}^2\tau = \frac{T_e}{m_e\nu_e}. \tag{1.4.2}$$

Since the diffusion coefficient of ions will also have a $mass^{-1}$, and a helium ion has 10^3 the mass of an electron this suggests that electrons should diffuse down their concentration gradients at a much faster rate. If this did occur an ionised gas would quickly become positively charged; this does not happen because as electrons exit a region, they leave a net positive charge behind which attracts negative charges and quickly reduces the electron flux. This effect is called *ambipolar diffusion.*

Overall, the electrical force experienced by electrons in the plasma and drag force due to momentum loses, will balance:

$$\mathbf{F_E} + \mathbf{F_{Friction}} = \mathbf{0} = -e\mathbf{E} - m_e \frac{\mathbf{u}_e - \mathbf{u}_i}{\tau_e}. \tag{1.4.3}$$

Due to quasineutrality, the electric field must impart equal and opposite momentum to the ions:

$$m_i \mathbf{u}_i = -m_e \mathbf{u}_e. \tag{1.4.4}$$

Because of the disparity in masses between ions and electrons, it is clear from Eq. (1.4.4) that the velocities of the ions are much lower. This means that Eq. (1.4.3) can be rewritten as:

$$-e\mathbf{E} - m_e \frac{\mathbf{u}_e}{\tau_e} = \mathbf{0}, \tag{1.4.5}$$

and there for the flux can be expressed as:

$$\Gamma_e = n_e \mathbf{u}_e - D_e \nabla n_e = -n_e e\mathbf{E}/m_e \nu_e - D_e \nabla n_e. \tag{1.4.6}$$

where $\nu_e = \tau_e^{-1}$. This can be simplified introducing the *electron mobility*, μ, defined as follows:

$$\mu = \frac{e}{m_e \nu_e}, \tag{1.4.7}$$

to

$$\Gamma_e = -n_e \mu_e \mathbf{E} - D_e \nabla n_e \tag{1.4.8}$$

Writing the ion flux in the same fashion and equating the two fluxes to maintain quasineutrality gives:

$$\Gamma_e = -n_e \mu_e \mathbf{E} - D_e \nabla n_e = n_i \mu_i \mathbf{E} - D_i \nabla n_i = \Gamma_i \tag{1.4.9}$$

Using quasineutrality to assume that $n_i \approx n_e \approx 0$ and rearranging to get an expression in terms of the electric field gives

$$\mathbf{E} = \frac{D_i - D_e}{\mu_i + \mu_e} \frac{\nabla n}{n}. \tag{1.4.10}$$

Substituting Eq. 1.4.10 into the expression for Γ_i in Eq. 1.4.9 gives

$$\Gamma = n\mu_i \frac{D_i - D_e}{\mu_i + \mu_e} \frac{\nabla n}{n} - D_i \nabla n. \tag{1.4.11}$$

Overall this allows Γ to be rewritten in the form:

$$\Gamma_{ambipolar} = D_{ambipolar} \nabla n, \tag{1.4.12}$$

where $D_{ambipolar}$ is shorthand for:

$$D_{ambipolar} = \frac{\mu_e D_i + \mu_i D_e}{\mu_i + \mu_e}. \tag{1.4.13}$$

Noting that$\mu_e \gg \mu_i$, it can be seen that the rate of diffusion is dominated by the slower species, the ions. Eq. (1.4.14) can be simiplified to

$$D_{ambipolar} \approx D_i + \frac{\mu_i}{\mu_e} D_e. \tag{1.4.14}$$

1.4.2 Diffusion in an magnetised plasma

A magnetic field adds a preferred direction to the motion of charged particles. Motion parallel to a $\mathbf{B}$ field in the $\hat{\mathbf{z}}$ direction will still be governed by Eq. (1.4.8):

$$\Gamma_z = \pm n\mu E_z - D\frac{\partial n}{\partial z}. \tag{1.4.15}$$

This holds for both species.

In the directions perpendicular to the direction of the magnetic field the equation of motion gains a term:

$$mn\frac{d\mathbf{v}_\perp}{dt} = \pm en(\mathbf{E} + \mathbf{v}_\perp \times \mathbf{B}) - T\nabla n - mn\nu\mathbf{v}. \tag{1.4.16}$$

Because of these extra terms, the expressions for Γ_x and Γ_y are modified as follows:

$$\Gamma_x = \pm n\mu E_x - D\frac{\partial n}{\partial x} \pm n\frac{\omega_c}{\nu}v_y, \tag{1.4.17}$$

and

$$\Gamma_y = \pm n\mu E_y - D\frac{\partial n}{\partial y} \pm n\frac{\omega_c}{\nu}v_x. \tag{1.4.18}$$

Since $\Gamma_y = nv_y$ and $\Gamma_x = nv_x$ it is possible to substitute for v_x in Eq. 1.4.18 above. This gives:

$$v_y(1 + \frac{\omega_c^2}{\nu^2}) = \pm\mu E_y - \frac{D}{n}\frac{\partial n}{\partial y} - \frac{\omega^2}{\nu^2}\frac{E_x}{B} \pm \frac{\omega^2}{\nu^2}\frac{T}{eB}\frac{1}{n}\frac{\partial n}{\partial x} \tag{1.4.19}$$

,

and similarly v_x can be expressed as

$$v_x(1 + \frac{\omega_c^2}{\nu^2}) = \pm\mu E_x - \frac{D}{n}\frac{\partial n}{\partial x} + \frac{\omega^2}{\nu^2}\frac{E_y}{B} \mp \frac{\omega^2}{\nu^2}\frac{T}{eB}\frac{1}{n}\frac{\partial n}{\partial y} \tag{1.4.20}$$

.

The second last terms of Eq. (1.4.19) and Eq. (1.4.20) can be identified with the $\mathbf{E}\times\mathbf{B}$ drift and the last terms of these two equations can be recognized as the diamagnetic drift.

By defining the perpendicular mobility as:

$$\mu_\perp = \mu\frac{1}{1 + \omega_c^2\tau^2}, \tag{1.4.21}$$

and the perpendicular diffusion coefficient as

$$D_\perp = D\frac{1}{1 + \omega_c^2\tau^2}, \tag{1.4.22}$$

where $\nu^{-1} = \tau$, the two equations Eq. (1.4.19) and Eq. (1.4.20)can be rewritten in a clearer vector form as:

$$\mathbf{v}_\perp = \pm\mu_\perp\mathbf{E} - D_\perp\frac{\nabla n}{n} + \omega_c^2\tau^2\frac{\mathbf{v_E} + \mathbf{v_D}}{1 + \omega_c^2\tau^2}. \tag{1.4.23}$$

The first two terms in Eq. (1.4.23) correspond to the terms in Eq. (1.4.8) but with the factor of $1 + \omega_c^2\tau^2$ in the denominator which yields Eq. (1.4.8) when $\tau = 0$. These terms act parallel to electric field and the gradient in density. The last term is caused

by the presence of a magnetic field and leads to drifts perpendicular to the **E** field and the density gradient.

The presence of a **B** reduces the amount of drift and diffusion in the direction of **E**; the parameter $\omega_c^2\tau^2$ determines how much of a reduction occurs. When $\omega^2\tau^2 \gg 1$ it is clear that the magnetic field will dominate the process and will significantly slow diffusion along **E**.

In the case of $\omega^2\tau^2 \gg 1$ the diffusion coefficient is given by

$$D_\perp = D\frac{1}{\omega_c^2\tau^2} = \frac{T}{m\nu}\frac{1}{\omega_c^2\tau^2} \sim \frac{r_L^2}{\tau}. \tag{1.4.24}$$

Showing that as expected the appropriate length step in magnetised plasmas is the Larmor radius.

It is worth noting that the relationship between the mass and the diffusion coefficient differs for motion along and perpendicular to the magnetic field; since $\tau \propto m^{1/2}$ it can be seen that $D \propto m^{-1/2}$ whereas $D_\perp \propto m^{1/2}$. When particles are moving parallel to the magnetic field the electrons have a larger diffusion coefficient and therefore travel faster whereas the heavier ions move more slowly, in the case of motion across a magnetic field however the ions are able to diffuse more quickly due to their larger larmor orbits.

1.4.3 Ambipolar diffusion in a magnetized plasma

The concept of ambipolar diffusion can also be applied in the case of magnetised plasmas, but its implementation is non trivial [1][4] due to fact that the problem is no longer isotropic - the presence of a **B** field provides a preferred direction for motion.

It is possible that in a magnetised plasma, the ions and electrons may exit the plasma using two different paths. The ions, as was shown above, can diffuse radially faster than the electrons, but the electrons may not diffuse radially to cancel out the resulting charge imbalance. Instead the electrons may travel along the field lines. The overall quantity that must be kept in balance is not the flux through a surface, $\mathbf{\Gamma}$, but rather the divergence of the flux $\boldsymbol{\nabla}.\mathbf{\Gamma}$. This is not a trivial problem since it involves setting $\boldsymbol{\nabla}.\mathbf{\Gamma}_i = \boldsymbol{\nabla}.\mathbf{\Gamma}_e$, where $\mathbf{\Gamma}_i$ is given by

$$\boldsymbol{\nabla}.\boldsymbol{\Gamma}_i = \boldsymbol{\nabla}_\perp.(\mu_i n\mathbf{E}_\perp - D_{i\perp}\boldsymbol{\nabla}n) + \frac{\partial}{\partial z}\left(\mu_i n E_z - D_i\frac{\partial n}{\partial z}\right), \tag{1.4.25}$$

and $\boldsymbol{\Gamma}_e$ by

$$\boldsymbol{\nabla}.\boldsymbol{\Gamma}_e = \boldsymbol{\nabla}_\perp.(-\mu_e n\mathbf{E}_\perp - D_{e\perp}\boldsymbol{\nabla}n) + \frac{\partial}{\partial z}\left(-\mu_e n E_z - D_e\frac{\partial n}{\partial z}\right). \tag{1.4.26}$$

2. EXPERIMENTAL APPARATUS

2.1 Double plasma vessel

The apparatus used in this research was the Double Plasma Device pictured below in Fig. 2.1. This vessel consisted of two chambers, the red chamber and the cylindrical chamber. Only the cylindrical chamber was employed in this investigation. The cylindrical vessel has an internal diameter of 24.7 cm and a length of 46 cm. The inlet for helium, the substrate gas, is in the red chamber, and the outlet to the pumps is in the base of the cylindrical chamber. The outlet is protected by a mesh filter to prevent large detritus from the filament or the Langmuir probe damaging the turbomolecular pump.

2.2 Pumps

The creation of the low pressure environment is achieved using two different pumps - a rotary vane pump and a turbomolecular pump. The rotary vane pump is a *Pfeiffer Balzers Duo 016B* model which spins at 300 rev/s and reduces the pressure to roughly 10^{-2} mbar. This pump operates by rotating a moveable vane mounted on a cylinder within a larger cylinder. The axes of the two cylinders are offset from each other which draws the gas from the chamber as each vane passes the inlet as depicted in Fig 2.2.

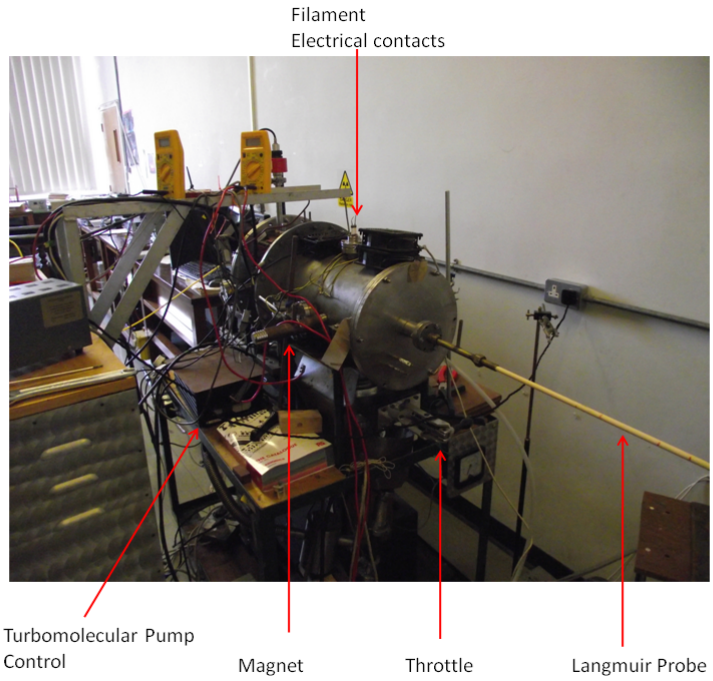

Fig. 2.1: Double plasma vessel

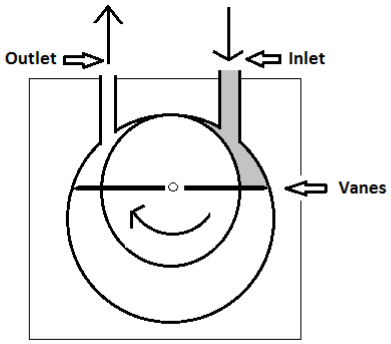

Fig. 2.2: Rotary vane pump

The turbomolecular pump, a *Leybold Turbovac 361*, is controlled by a *Turbotronik NT20*. The turbomolecular pump operates on the principle of conservation of momentum; a series of collisions with finely positioned layers of fan blades directs molecules downwards from the gas above. The turbomolecular pump will only work if the starting pressure is already low, hence the need for the rotary vane pump. It reduces the pressure to roughly 10^{-6} mbar.

2.3 Pressure gauges

Three pressure gauges were used in this apparatus - a *Pirani* gauge, a *Penning* gauge and a *Baratron* gauge. The Pirani gauge is the least sensitive gauge and was only used during the creation of a vacuum to determine when the pressure had fallen sufficiently to allow the turbomolecular pump to be activated. The Pirani is accurate to a pressure of roughly 10^{-2} mbar. Pirani gauges work like a Wheatstone bridge; a fall in pressure changes the resistance across one resistor of the bridge, unbalancing the bridge and causing a current to flow. The current which flows can be related to the pressure in the system. The Penning gauge is a more sensitive measuring device for low pressure environments. It utilises cold cathode ionization to produce electrons which subsequently travel in long spiral trajectories in a magnetic field before colliding with the anode, where their probability of causing an ionisation and therefore contributing a positive ion to the current in the circuit is given by

$$i_+ = kp^n, \tag{2.3.1}$$

where k and n are properties of the gas in use. The Penning needs to be calibrated for the gas in use, and the calibration factor in helium is roughly 5.9. The Baratron gauge works on the principal of a capacitor with a moveable plate; as the pressure increases or decreases, one plate moves towards, or away, from the other, changing the capacitance of the system. The change in capacitance provides a measure of the change in pressure. The pressure measured by a Baratron gauge does not require calibration for each gas.

2.4 Magnets

The magnetic mirror is created using two columns of cylindrical permanent magnets made from an NdFeB alloy. Four magnet diameters were available: 11 mm, 23 mm,30 mm and 50 mm allowing a range of possible magnetic field profiles. These magnets consisted of stacks of flat cylindrical magnets, thus allowing an extra degree of freedom for the choice of field - it was possible to use shorter columns of the 11 mm magnets. Normally the stacks of magnets were 20 cm long. The magnets were held in place with moveable stands allowing the position of the magnetic mirror to be moved with respect

Magnet diameter(mm)	B(mT)
50mm	5.67
30mm	2.10
23mm	1.24
11mm	0.29

Tab. 2.1: Magnetic flux density at the vessel centre.

to the filament. The maximum field strength on the flat surfaces was 0.65 T which means that the internal field is 1.3 T.

Using a modified version of code provided by Dr. McCarthy, the strength of the magnetic field created by two columns of cylindrical magnets arranged axi-symmetrically was plotted as a function of distance along that axis. As can be seen in Fig 2.3, the magnetic field diminishes quickly just inside the walls of the vessel; it falls from roughly 600 mT at the walls ($z = 0.00$ m and $z = 0.25$ m), to less than 6 mT at the vessel centre ($z = 0.125$ m). The values of the magnet flux density at the vessel centre are given in Table (2.4)

The fall off is relatively steep for the smaller radius magnets, and more gradual for the larger ones(see Fig. 2.3), as would be expected based on a simple treatment of the magnets as a solenoid.

The Larmor radius (given by Eqn. 1.3.8 with the velocity given by the square root of the temperature with the appropriate multiplier) at the vessel centre, assuming a magnetic field of 5.67 mT and an electron temperature of 3 eV, will be roughly 1 mm which is significantly thicker than the probe radius.

2.5 The filament and associated circuits

The plasma was generated by the discharge of electrons from a heated, negatively biased filament which was mounted in the roof of the cylindrical chamber (see Fig 2.4). The filament consisted of a single 0.38 mm tungsten wire, approximately 20cm long. The filament was mounted onto two 3 mm diameter copper wires which connected to dual

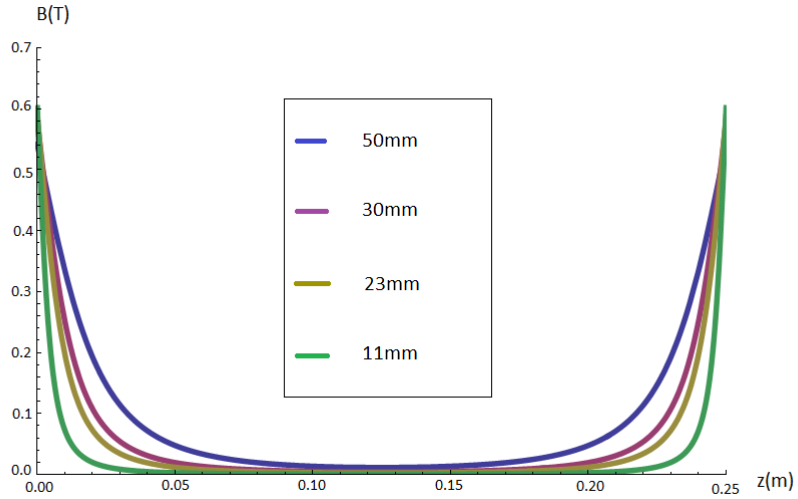

Fig. 2.3: Strength of magnetic field along axis of magnetic mirror

insulated electrical feed-thru's in a vacuum flange. The filament had a roughly circular shape, details of which varied each time the filament was replaced. The filament was oriented such that a Langmuir probe, scanned axially, could pass through the centre.

On operation, a DC current of up to 18 A was passed through the filament providing ohmic heating of the filament. On heating, thermionic emission of electrons from the filament occurred. The filament was additionally biased to a negative voltage of as large as -400 V with respect to the chamber walls. Heating and bias power are provided by *Farnell H60/50* and *DeltaElektronica SM400-AR-8* power supplies, respectively.

The bias voltage accelerated the free (emitted) electrons. This current from the filament to the chamber walls is called the *plasma current*. The energetic electrons collided with the helium in the chamber causing ionisation. In the ionisation event the energetic electron lost energy (24 eV for helium) and the helium atom converted to a (cold) electron-ion pair. Theses e-ion pairs form the bulk of the plasma. The resultant plasma consists of a minority beam-electron component from the filament, a majority plasma-electron component, and a helium-ion component to preserve quasi-neutrality.

Collisions within the plasma-electron population resulted in an approximately Maxwellian energy distribution, and we ascribe the electron temperature, T_e to this value. Both the beam-electrons and plasma-electron can cause electronic excitation of the helium gas,

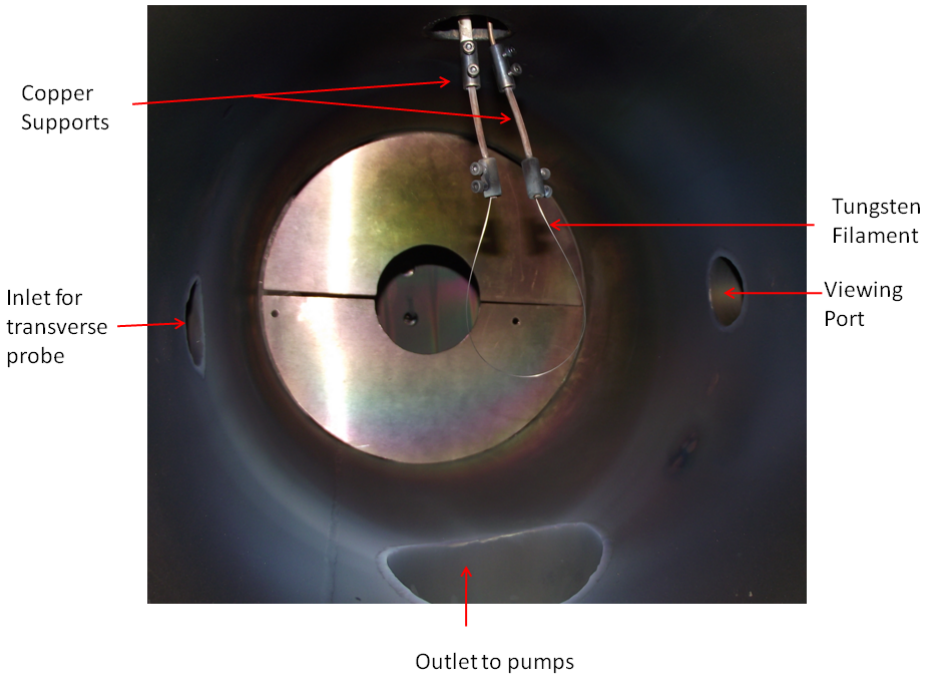

Fig. 2.4: Interior of double plasma vessel showing filament

and the resultant de-excitation gives rise to the optical emission spectra.

Typical experimental conditions are listed in Table 2.5.

Data collection with the Langmuir probe close to the filament was limited (typically to currents below 2A) due to the risk of damage which could be caused by arcing between the filament and the Langmuir probe, and heat-load onto the insulators from the filament.

The filament was heated using a *Farnell H 60/50* power supply, which ensured that heating (filament) currents of 18 A could be supplied when needed. The bias was applied using a *Delta Elektronica SM 400- AR-8* , this allowed for plasma currents of up to $8A$ and bias voltages of up to 400 V. The range of engineering parameters used during operation is given in Table (2.5) Typically the pressure did not exceed 2.5 mTorr except during pressure scans to minimize the strain on the turbomolecular pump, the plasma current was usually kept significantly below 2 A to preserve the filament and to protect the Langmuir probe from damage. The size of the heating current used depended on the age of the filament, and was dramatically decreased as the filament reached the end

Parameter	Min.	Max.
Pressure(mTorr)	0.1	16
Bias Voltage(V)	40	200
Heating Current(A)	12.5	17.5

Tab. 2.2: Engineering parameters

of its lifespan.

2.6 The window

The window consisted of fused quartz with a diameter of 30 mm and was held in place with bolts. A seal was maintained using an O ring. The window became progressively stained during long experimental runs. This interfered with spectroscopic measurements because the optical transmission fell by up to 90%. The window was cleaned using a solution of nitric acid.

2.7 The spectroscope and associated code

The spectroscope used in this research was an *OceanOptics USB2000* model. This spectroscope provided usable data in the wavelength range between 300 nm and 750 nm. The associated software output each time-averaged spectrum as an ascii text file which was subsequently imported into a Mathematica program for data processing. The raw data was then corrected to take into account the background count black body emission from the filament and the differing sensitivities of the spectroscope over its ranged of usable wavelengths. An example of an uncorrected spectrum acquired during the experimental work is shown in Fig. 2.5

The removal of the background was handled by the Mathematica code I wrote to process each spectrum file (see Appendix). The location of peaks and number of data bins which corresponded to each peak was determined in trial scans. A set number of data bins on either side of each peak were specified in the code and a linear interpolation was made between the two sets of points - see Fig. (2.6). This linear fit was used to

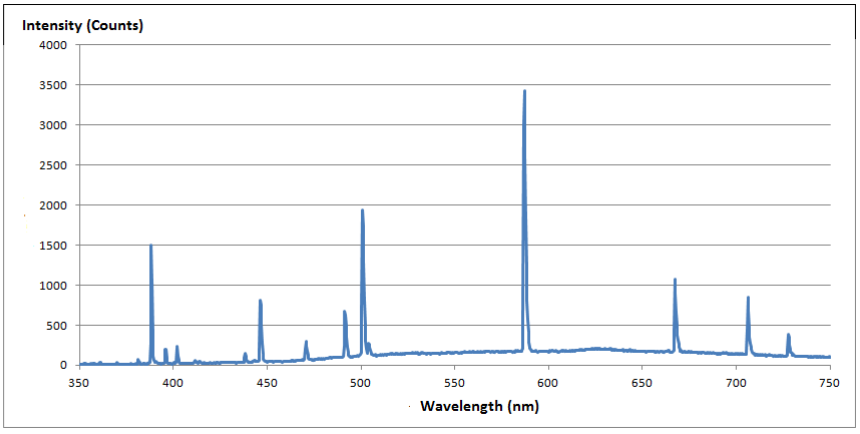

Fig. 2.5: Sample spectrum showing background and emission peaks

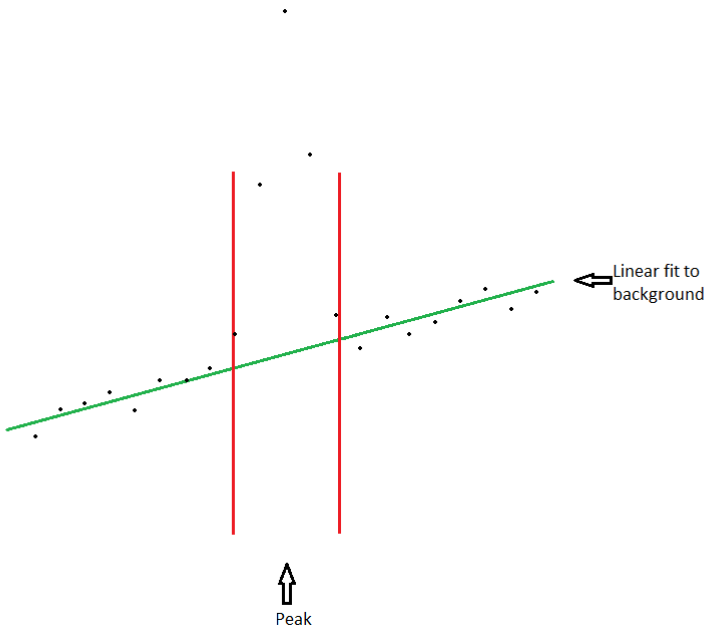

Fig. 2.6: Procedure for removing background

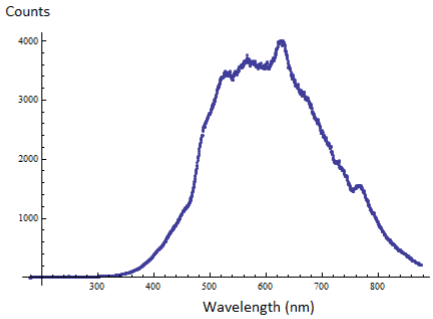

Fig. 2.7: Background

calculate notional noise estimations for the bins occupied by the peaks and this value was then subtracted from the actual value in the bin to provide a measure of the peak strength.

By comparing a sample blackbody spectrum (Fig. 2.7) obtained using the device and a blackbody lamp to the theoretical behaviour of a black body over the same range of wavelengths it was possible to find correction factors for each wavelength bin used. These factors were subsequently used to normalise the peak intensities to compensate for the non uniform spectroscopic sensitivity across the wavelength range. This processing was implemented by the mathematica code.

2.8 The Langmuir probe

The theory of Langmuir probes is covered in chapter 3. In this section, I will describe the design of the probe used during this research.

2.8.1 Construction

There were two possible ways to insert a Langmuir probe into the vessel; the main probe used in this research was the *axial probe* which was inserted along the axis of the cylindrical vessel. The other probe was inserted perpendicular to the axis of the cylinder at a position 23.5 cm from the end plate of the vessel, this was called the *radial probe*. The flange around the radial probe did not produce a strong enough seal and the use of this probe was discontinued after several attempts to resolve this issue.

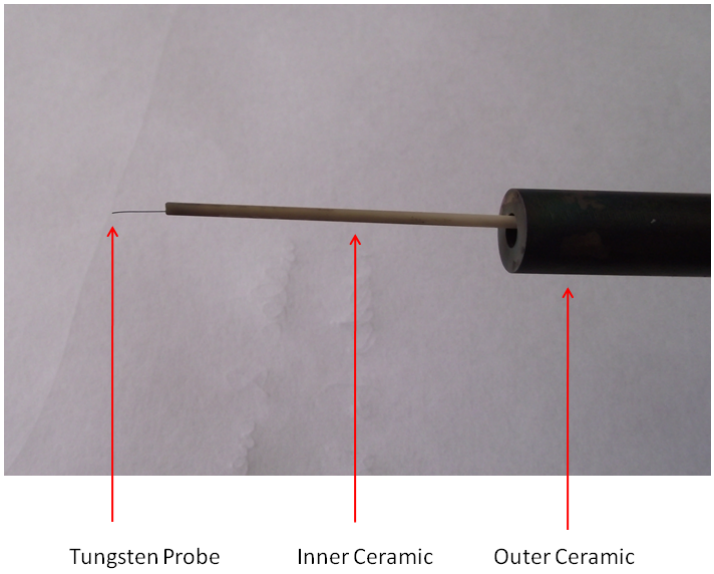

Fig. 2.8: Picture of Langmuir probe

Several Langmuir probes, each of the same basic construction, were used in the course of these experiments. The basic design is depicted in Fig. (2.9). The cylindrical probe consisted of a tungsten wire of diameter 0.1 mm soldered onto a thicker wire, of diameter 1 mm, which was attached to the signal generator circuit outside the vessel. Only the last 7 or $8mm$ was left exposed. The section between this and the heavier wire was shielded by a thin ceramic tube, with an external diameter of 1.6 mm and length of 55 mm. The heavy wire was, in turn, contained within a ceramic tube of length 1 m and external diameter of 10 mm. This design allowed the distance the probe was inserted into the vessel to be varied, and also allowed the probe to be rotated through a full turn if needed. The use of the thin and thick ceramic tubes ensured that only the exposed tungsten acted as an electrode, and served to minimise the perturbation of the the plasma by the Langmuir probe.

The design of the probe was varied over the duration of the data collection process. The main innovation was to increase the surface area of the wire within the inner ceramic by wrapping the tungsten probe wire around a thin copper wire or using several tungsten probe wire pieces wound together. Only the shape of the exposed probe wire was varied; configurations perpendicular to the ceramic and parallel were both explored.

The probe circuit is depicted in Fig. 2.10. The function generator used was a *Thurlby*

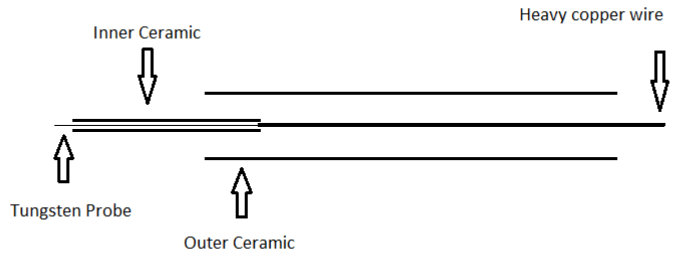

Fig. 2.9: Schematic of axial Langmuir probe

Thandar Instruments TG 550. Two of its waveforms were used extensively - the sinusoidal signal and the sawtooth signal. The sawtooth signal had the advantage of a more even distribution of the data points in time, whereas the data with the sinusoidal signal was clustered towards the flatter parts of the waves. The signal generator allowed several different frequencies to be chosen. For most of this work, the choice of signal frequency was 50 Hz. The amplitude of the signal was usually around 100 V, and the resulting current was kept below 60 mA to avoid melting the probe.

The voltage applied to the probe was measured using channel A of the *Picoscope* and the resulting current was measured with channel B. The resistance used in the circuit was varied, but was set at 1000 Ω for the collection of most of the data employed the analysis chapter.

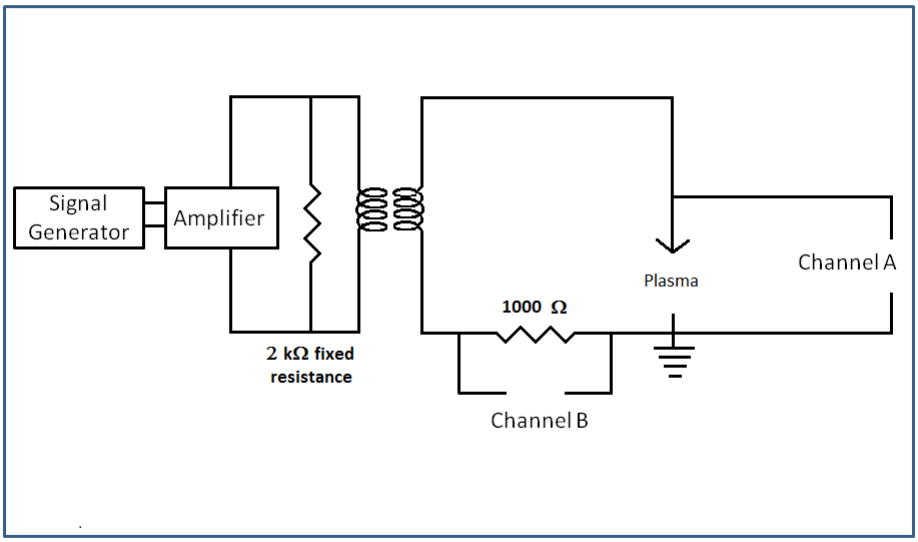

Fig. 2.10: Circuit diagram of probe and Picoscope channels

3. SHEATHS AND LANGMUIR PROBE THEORY

This chapter is based heavily on the the introductory texts by Chen[1], Boyd and Sanderson[4], Bellan [3], the books on diagnostics and probes by Swift and Schwar [11], and Hutchinson [8], together with the fundamental papers on Langmuir probe by Langmuir et al. [7], and the paper on charge exchange currents by Sternovsky et al. [6].

3.1 Sheaths

When a plasma comes into contact with a conducting wall or probe a region called a sheath forms. The reason for sheath formation can be seen by examining the flux equation obeyed by particles in a plasma:

$$\Gamma_{th} = \frac{1}{4} n_{i,e} \overline{v}_{th}, \tag{3.1.1}$$

where Γ is the flux of particles, $n_{i,e}$ is the density of electrons or ions, and $\overline{v}_{th}$ is the average thermal speed of the given species. If the particle velocities obey Maxwell Boltzmann statistics, then the average speed is found by integrating the product of the speed and the distribution function over all possible speeds. This yields:

$$\overline{v} = \int_0^\infty v f(v) dv = \int_0^\infty \sqrt{\frac{2}{\pi}\left(\frac{m}{T_e}\right)^3} v^3 \exp\left(\frac{-mv^2}{2T_e}\right) dv = \sqrt{\frac{8T_e}{\pi m_e}}, \tag{3.1.2}$$

where T_e is the temperature of the electrons. It is clear that the mean speed of a species is inversely proportional to the square root of its mass, and, consequently, that ions will travel an order of magnitude more slowly than electrons. If no change in potential occurs near the wall or probe, then the plasma would quickly be depleted of electrons. Instead as the probe or wall charges up negatively with respect to the plasma, electrons will be repelled back into the bulk of the plasma. The height of this barrier

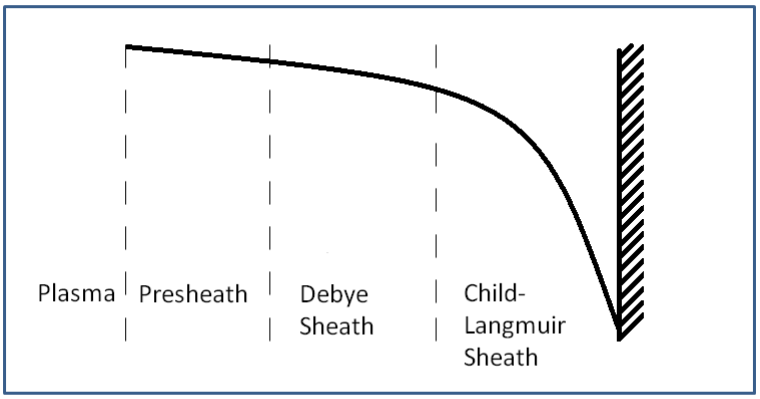

Fig. 3.1: Regions of sheath

will adjust until the two fluxes equalise. In this scenario, lower energy electrons will not be able to reach the wall. Fig. 3.1 shows the variation in potential near a wall or probe. The regions of the potential variation will be examined after an investigation of the critical velocities involved.

If the velocity of an ion far from the wall is u_0, then the conservation of energy yields[1]:

$$\frac{1}{2}mu^2 = \frac{1}{2}mu_0^2 - e\phi(x). \tag{3.1.3}$$

Using the equation of continuity for the ions,

$$n_0 u_0 = n_i(x)u(x), \tag{3.1.4}$$

gives:

$$n_i(x) = n_0\left(1 - \frac{2e\phi}{mu_0^2}\right)^{-1/2}. \tag{3.1.5}$$

The density of electrons may be expressed using the Boltzmann relation as:

$$n_e(x) = n_0 \exp(\frac{e\phi}{T_e}). \tag{3.1.6}$$

Now using Eq. (3.1.5), and Eq. (3.1.6) Poisson's relation for the potential becomes:

$$\frac{d^2\phi}{dx^2} = \frac{en_0}{\epsilon}\left[\exp\left(\frac{e\phi}{T_e}\right) - \left(1 - \frac{2e\phi}{mu_0^2}\right)^{-1/2}\right]. \tag{3.1.7}$$

Multiplying Eq. (3.1.7) by $\frac{d\phi}{dx}$ allows it to be integrated by parts as follows:

$$\int_0^x \frac{d^2\phi}{dx^2}\frac{d\phi}{dx} = \left[\frac{d\phi}{dx}\frac{d\phi}{dx}\right]_0^x - \int_0^x \frac{d^2\phi}{dx^2}\frac{d\phi}{dx}. \tag{3.1.8}$$

Both the potential and its derivative, the electric field, can be taken to be zero at $x = 0$, which allows the integral of Eq. (3.1.7) to be written as

$$\frac{1}{2}(\frac{d\phi}{dx})^2 = \frac{n_0}{\epsilon_0}\left(\frac{m_i u_0^2}{T_e}\left([1 - \frac{2e\phi}{m_i u_0^2}]^{1/2} - 1\right) + \exp^{\frac{e\phi}{T_e}} - 1\right). \tag{3.1.9}$$

The right hand side must be positive and when Taylor expanded[1] in the region where ϕ is small it gives the following:

$$\left(-\frac{T_e}{m_i u_0^2} + 1\right) \geq 0, \tag{3.1.10}$$

which is called the *Bohm criterion*. Hence there is is a critical velocity, the *Bohm Velocity*:

$$u_B = \left(\frac{T_e}{m_i}\right)^{1/2}. \tag{3.1.11}$$

Ions need to have speeds exceeding the Bohm velocity to reach the wall or probe. This velocity is also the speed of sound for ions. Hence in the sheath the ions are supersonic. The implication is that outside the sheath, there must be a region called the *presheath* in which the ions are accelerated to the required velocity by a potential drop given by examining the conservation of energy:

$$e\phi \geq \frac{1}{2}m_i u_B^2. \tag{3.1.12}$$

Hence

$$\phi \geq \frac{1}{2}\frac{T_e}{e}. \tag{3.1.13}$$

Clearly the density of electrons given by Eq. (3.1.6) is negligible close to the wall and therefore the electron term in Eq. (3.1.7) can be neglected and integrating again it can be shown[1] that this region has a thickness,d, given by:

$$d = \frac{2}{3}\left(\frac{2\phi_w^3}{em_i}\right)^{1/4}\sqrt{\frac{\epsilon_0}{n_0 U_B}}, \tag{3.1.14}$$

where ϕ_w is the potential at the wall. This region is called the *Child Langmuir sheath.*

The region between the presheath and the Child Langmuir Sheath has an exponentially increasing electron density in the outward direction and has a scale comparable to the Debye Length; the electron velocities in this region are largely isotropic apart from the few high energy electrons which make it to the wall/probe and which are absorbed there, the velocities of the ions in this region are directed towards the wall.

The sheath was modelled [10] by interpolating solutions to Poisson's equation in cylindrical coordinates:

$$\frac{1}{r}\frac{\partial}{\partial r}\left(r\frac{\partial V}{\partial r}\right) = -\frac{ne}{\epsilon_0} \tag{3.1.15}$$

where density, n, is given by

$$n = n_0 - n_h \exp^{\frac{eV}{T_h}} - n_c \exp^{\frac{eV}{T_c}} \tag{3.1.16}$$

Where n_0 is the ion density, n_h the hot electron density, n_c the cold electron density, T_c the cold electron temperature and T_h the hot electron temperature.

The sheath thickness, x_s, satisfies the equation:

$$x_s = \lambda_D\sqrt{g_1(\rho)}fTanh[g_2(\rho)f^2] \tag{3.1.17}$$

where $\rho = r/\lambda_D$, with r being the probe radius. The functions $g_1(\rho)$ and $g_2(\rho)$ have the form

$$\begin{aligned} g_1(\rho) &= a_1 + b_1\sqrt{\rho} + c_1\rho + d_1\rho^3 \\ g_2(\rho) &= a_2 + b_2\sqrt{\rho} + c_2\rho + d_2\rho^3 \end{aligned} \tag{3.1.18}$$

where a_1, a_2, b_1, b_2, c_1, c_2, d_1 and d_2 are constants found by interpolation.

The function f has the following form;

$$f = -\frac{eV}{T_s}, \tag{3.1.19}$$

where T_s is a harmonic shielding temperature defined as follows:

$$\begin{aligned} h &= \frac{n_h}{n} \\ \frac{1}{T_s} &= \frac{h}{T_h} + \frac{1-h}{T_c}, \end{aligned} \tag{3.1.20}$$

h represents the hot electrons as a fraction of the total density of electrons.

3.2 Langmuir probe theory and computational implementation

A Langmuir Probe is a thin wire which is placed in the plasma, biased with a voltage using a signal generator, and used to collect a current which is subsequently analysed to provide information about the temperatures and densities of the species in the plasma.

3.2.1 Assumptions

The assumptions involved in Langmuir probe theory[11] are:

(a) The pressure involved is low enough that no collisions occur in the sheath region.

(b) Charge carriers are neutralised at the probe surface.

(c) Charge carriers are not emitted by the probe surface.

(d) The entire probe potential is developed across the sheath.

(e) The velocity profiles are known at the sheath edge.

(f) The effect of the supports on the probe are ignored.

(g) The probe is sufficiently small not to disturb the plasma.

(h) The densities of the electrons and ions are known at the sheath edge.

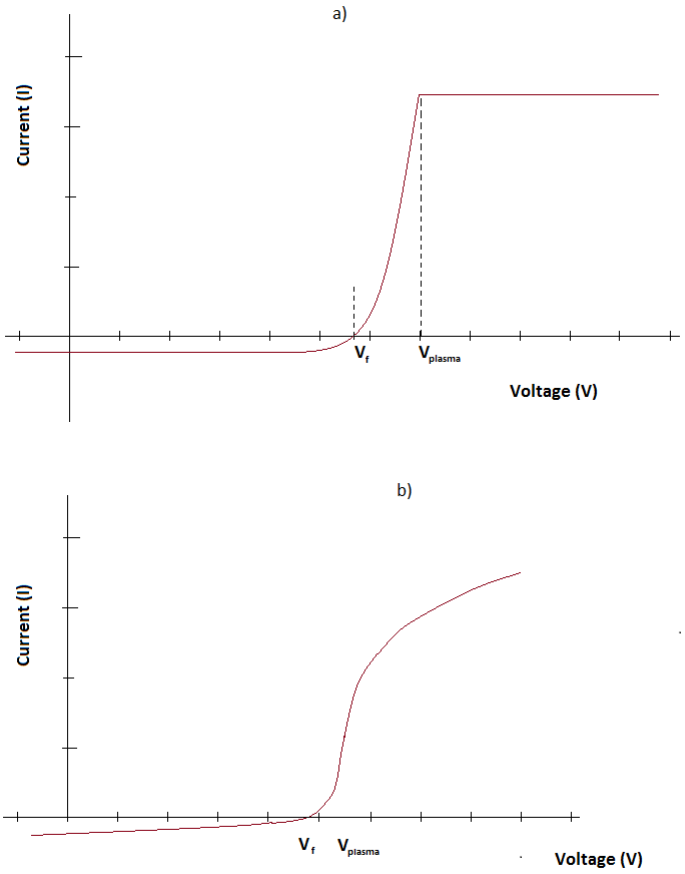

Fig. 3.2: a) Ideal characteristic b) Realistic characteristic

3.2.2 IV characteristics

The current collected by the probe is a function of the density of the charges flowing, the temperatures of these charges and their masses. The magnitudes of the ion current and electron current will differ significantly due to the differing masses of the ions and electrons. Fig. (3.2) shows how an ideal characteristic should appear and how an experimental characteristic actually appears.

Clearly there are three distinct regions in the idealised charactersitic: an ion current region, an electron current region and a transition region. As the probe becomes negatively biased it begins to repel electrons. At first only the least energetic electrons are affected but as the bias becomes more negative more electrons are repelled. A similar effect happens with the ions when the probe is positively biased.

Theoretically, both the electron and ion currents should saturate but in reality it is found that neither fully saturates because the dimensions of the sheath around the probe also change with the changing voltage, and, therefore, the area available to collect the current will also vary.

The voltage which corresponds to zero net current, i.e. where the ion current and electron current match each other, is called the *floating potential*, and is denoted by V_f. This is the potential which the probe would have if it were insulated from the rest of the system and allowed to charge up until no more current would flow to it.

The potential of the plasma in the absence of a probe is called the *plasma potential*, and is labelled as V_p. The plasma potential corresponds to the "knee" in the IV characteristic where the transition region ends and the electron dominated region begin.

3.2.3 Ion current

Ion saturation current

When the probe is highly negatively biased, i.e. when $V \ll V_p$, the current is composed solely of ions, and even the most energetic electrons are repelled. The current in this case is given by[4]:

$$\frac{1}{2} n_0 e A \left(\frac{2T_e}{\pi m_i} \right)^{1/2}. \tag{3.2.1}$$

OML current

Orbit Motion Limited Theory[7][11] is used to estimate the fraction of the incoming ions which will be collected by the probe. This fraction can be estimated by considering the angular momenta of incoming ions and using conservation of energy to express their velocities in terms of the potential difference through which they have moved. This is illustrated in Fig. 3.3.

The OML current collected by a cylindrical probe is given by:

$$I_{OML} = 4\pi R_p l n_0 e \left(\frac{T_i}{2\pi m_i} \right)^{1/2} \sqrt{\frac{e\pi\phi}{T_i}}, \tag{3.2.2}$$

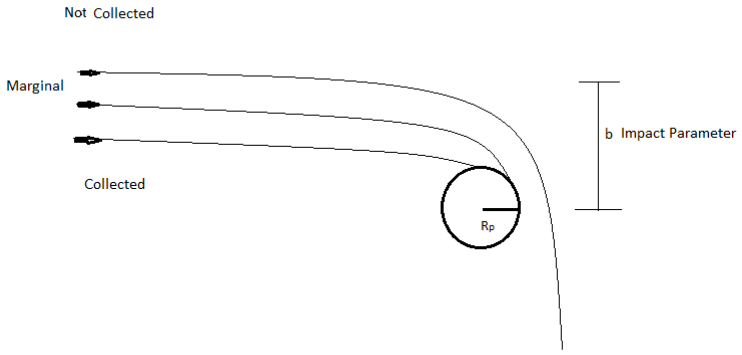

Fig. 3.3: Ion orbits

where ϕ is the potential of the probe relative to the surrounding plasma, T_i is the temperature of the ions, R_p is the radius of the probe and l is the exposed length of the probe.

Charge exchange current

The disparity between the current given by the OML theory and the current measured in experiments has led to modifications to the theory of current collection by the probe. In particular the addition of a charge exchange contribution[6] to the current. The concept in charge exchange collisions is that a collision within the sheath replaces a particle which was too energetic to be captured by the potential around the probe with one which is much slower and, hence, is captured. This significantly boosts the current which a probe collects. The charge exchange current can be expressed as follows[6]:

$$I_{CX} = 2\pi e n_n n_0 \int_{R_p}^{s} \sqrt{\hat{V}}\sigma_{CX}(\hat{V}) r dr, \tag{3.2.3}$$

where s is the sheath radius, n_n is the neutral density, l is the length of the probe, σ_{CX} is the charge exchange cross section which is species dependent and $\hat{V}$ is given by:

$$\hat{V} = \sqrt{\frac{-2e(V - V_P)}{M_i}}. \tag{3.2.4}$$

The dependence on the neutral density means that the charge exchange current

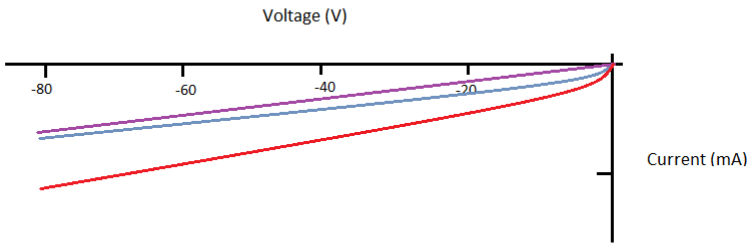

Fig. 3.4: The components of the ion current

should scale with the pressure.

Charge exchange collisions outside the sheath do not make an extra contribution to the ion current since they are largely accounted for by OML theory. Collisions in this region replace ions which may have been captured with ions which have the same capture probability.

Computational implementation

Since

$$I_{ion} = I_{CX} + I_{OML} \tag{3.2.5}$$

the ion component is modelled by adding the currents resulting from the two treatments above. This is allowable because the charge exchange interactions outside the sheath are already counted by OML Theory as explained above.

The red line in Fig. 3.4 represents the sum of the two contributions to the ion current; the OML current, I_{OML}, in blue and the charge exchange, I_{CX}, in purple.

3.2.4 Electron current

The electrons are divided into two distinct populations - a hot population with density n_h and temperature T_h, and a cold population with density n_c and temperature T_c.

When the probe is negatively biased, i.e. when $V < V_p$, the two populations follow the simple equation[10]:

$$i_{e,c/h} = \frac{n_{e,c/h} A}{4} \sqrt{\frac{8eT_{e,c/h}}{\pi m_e}} \exp^{\eta}, \tag{3.2.6}$$

where η is a shorthand for $\frac{V-V_p}{T_{e,c/h}}$. This equation decays exponentially as the probe repels more electrons as expected.

When $V > V_p$, the underlying equation for each species is more complicated[11][10]:

$$i_{e,c/h} = \frac{n_{e,c/h} A}{4} \sqrt{\frac{8eT_{e,c/h}}{\pi m_e}} \left(s(1 - Erfc\sqrt{\frac{\eta}{s^2 - 1}}) + \exp^{\eta} Erfc\sqrt{\frac{\eta}{1 - s^2}} \right), \tag{3.2.7}$$

where $s = r_{sheath}/R_p$.

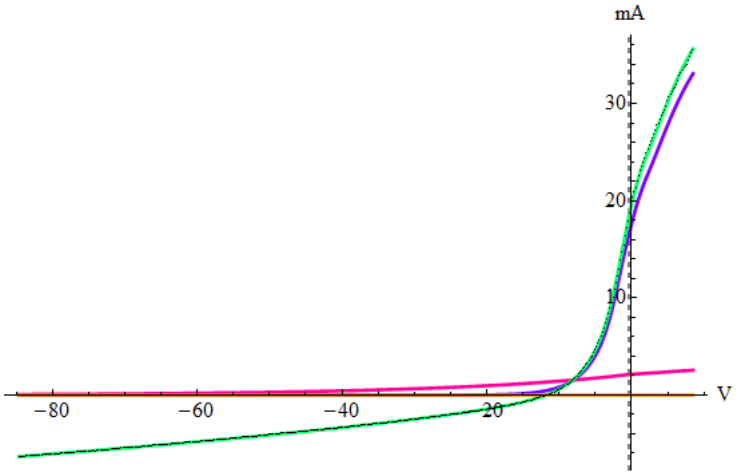

Fig. 3.5: Data with fitted model

3.2.5 Output

The overall output from the mathematica program is shown in Fig. (3.5). The green line is the fitted model. The purple and pink lines represent the cold and hot populations, respectively; this can be determined by noticing that the pink line remains sizeable for more negative probe bias, and, since high energy electrons can overcome a negative potential to reach the probe, this must necessarily correspond to the hot population.

4. RESULTS AND ANALYSIS

4.1 Examination of density and temperature along the axis of the vessel

The data shown in Fig. 4.1 and Fig. 4.2 depict the behaviours of the density of the cold and hot electron populations as the Langmuir probe collection area was manipulated incrementally along the axis of the vessel. The bias voltage during this experiment was fixed at 110 V, and the pressures used were: 1.2 mTorr, 2 mTorr, 3 mTorr, 4 mTorr and 6 mTorr. The confinement was provided by two columns of 30 mm permanent magnets. The axis of the magnetic mirror passed through the vessel centre, and set at 45^o to the horizontal to reduce staining of the viewing window. The vessel centre was located at 77.5 cm, and the centre of the plane of the filament was located at 76.0 cm.

The temperature of the cold population shown in Fig. 4.3 shows dramatically different behaviours for the different pressures at axial positions greater than 79 cm. It is probable that the true behaviour is closer to that of the 1.2 mTorr, 2 mTorr and 3 mTorr lines because the fitting programme has assigned spuriously high hot electron densities to the other two pressures at large distances from the vessel centre, as shown in Fig. 4.2, and low cold electron densities, as shown in Fig. 4.1. This suggests that the cold electron density declines only slightly over the range of axial positions examined.

The hot electron temperature profiles depicted in Fig. 4.4 shows an increase in the temperature of this population as the distance to the filament is decreased. The validity of the data points beyond 81 cm are questionable, particularly the rise in temperature found for the low pressure scans. The reason for these inconsistencies beyond 81 cm is that as the densities and temperatures converge in this region, it becomes more difficult to get a good fit to a two population model. The resulting hot temperatures at shorter distances from the filament also show that, the lower the pressure is, the higher the

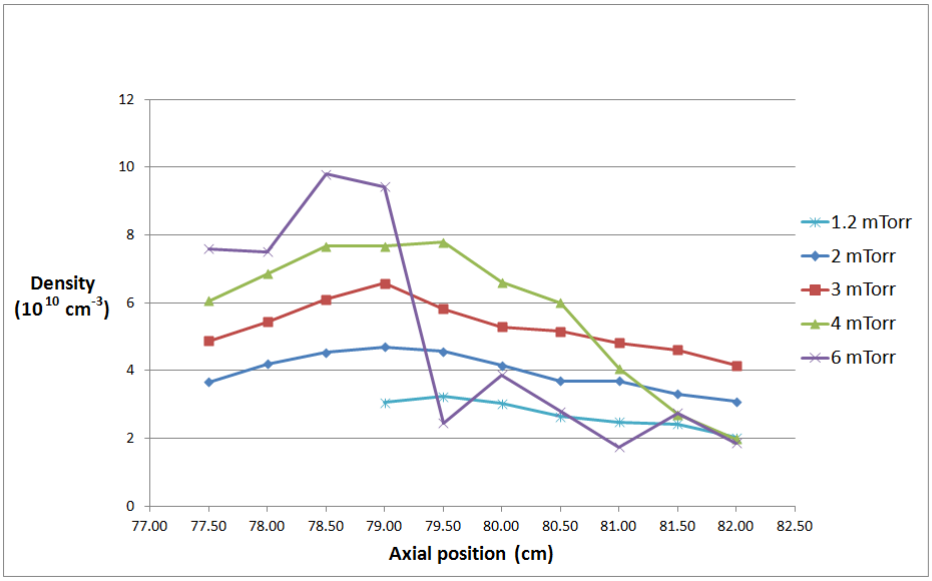

Fig. 4.1: The cold electron density for several pressures plotted against probe position

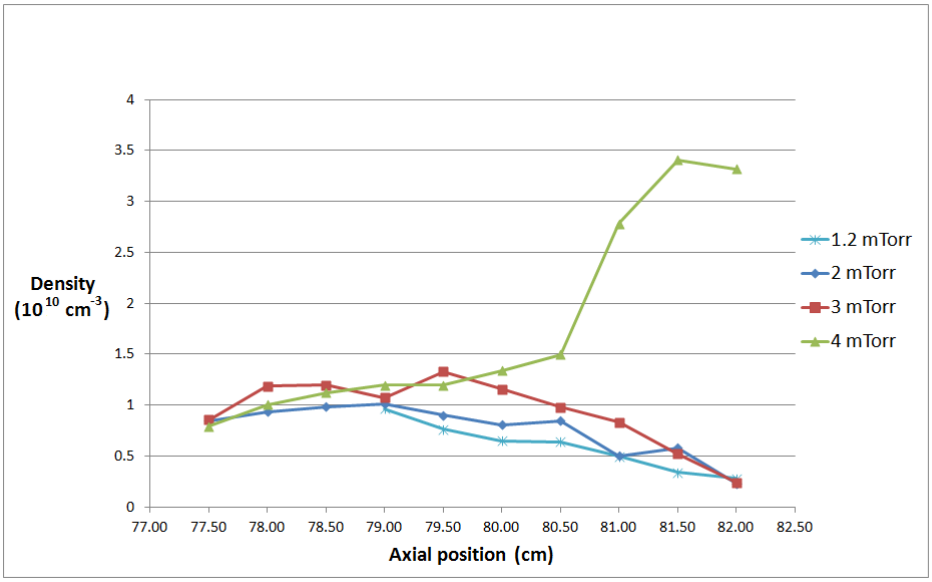

Fig. 4.2: The hot electron density for several pressures plotted against probe position

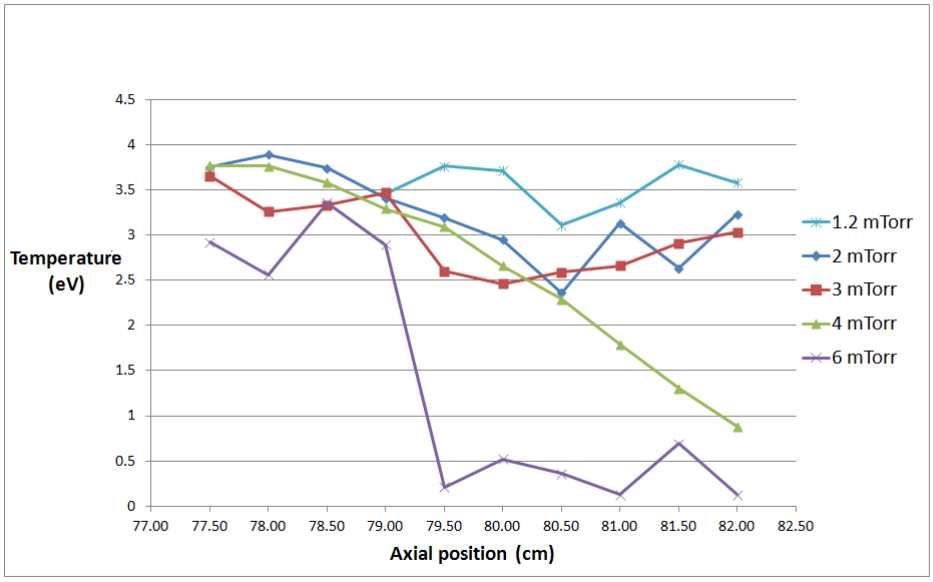

Fig. 4.3: The cold electron temperature for several pressures plotted against probe position

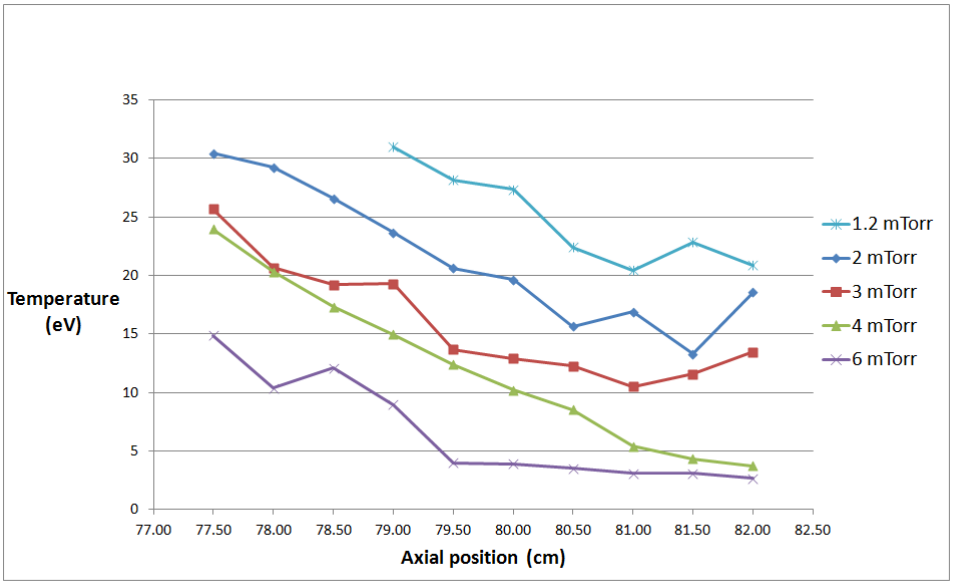

Fig. 4.4: The hot electron temperature for several pressures plotted against probe position

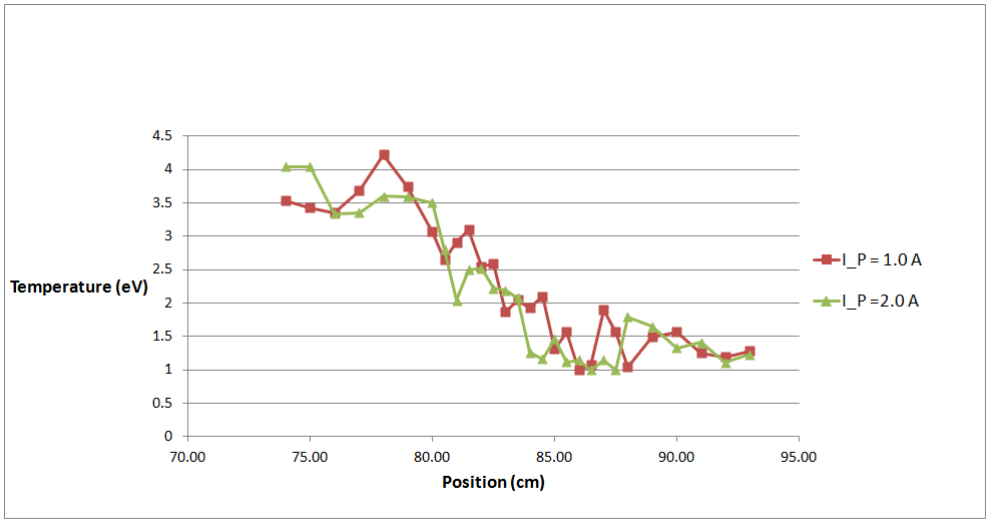

Fig. 4.5: The cold electron temperature for two plasma currents plotted against probe position

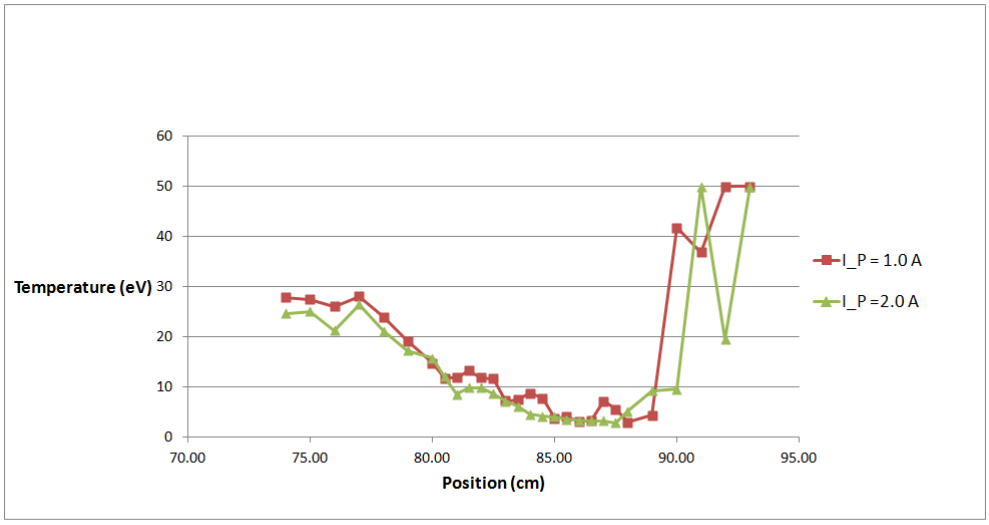

Fig. 4.6: The hot electron temperature for two plasma currents plotted against probe position

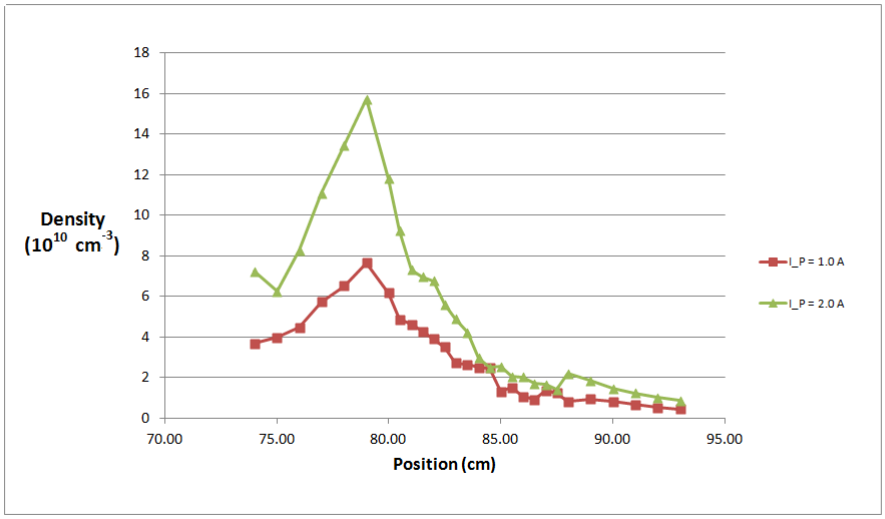

Fig. 4.7: The cold electron density for two plasma currents plotted against probe position

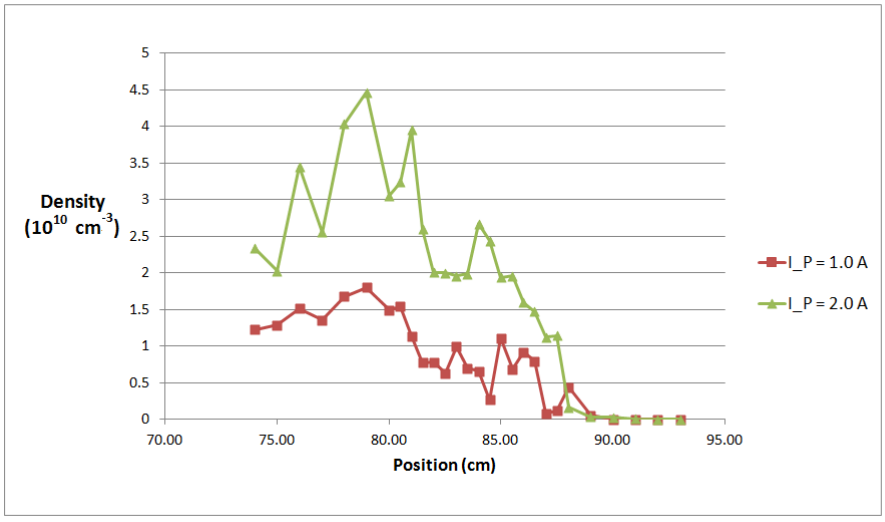

Fig. 4.8: The hot electron density for two plasma currents plotted against probe position

temperature of the electrons in the hot component of the electron population is.

The densities of the hot and cold populations both begin to decline at positions greather than 79cm, and both populations seem to have a maximum value near this. The peak in the cold density is more pronounced (as shown in Fig. 4.1). Nearer to the filament (position = 76.0cm), both populations show evidence of a trough. The slightly increased errors associated with the data in this region suggests that the failure to take beam effects into account may have given rise to lower densities being assigned to this region by the program. It is also possible that the nature of the paths of the electrons coming off the filament gives rise to an area of low electron density, as the electrons from one side of the filament loop would begin to be repelled by incoming electrons from the other side.

The peak density values are located at a point whose distance from the magnetic axis, D_{pc}, is given by:

$$D_{pc} \equiv Position_{peakdensity} - Position_{magneticaxis} = 1.5cm. \tag{4.1.1}$$

D_{pc} closely matches the distance,D_{fc}, from the magnetic axis, to the centre of the filament:

$$D_{fc} \equiv Position_{magneticaxis} - Position_{filamentcentre} = 1.5cm. \tag{4.1.2}$$

This symmetry about the magnetic axis suggests that a current may be flowing around the magnetic field forming a *ring current*. This is supported by the result shown in 1.3.33, which showed that particles would drift in the azimuthal direction around the axis of the magnetic mirror.

The unusual behaviour of the 6 mTorr line in Fig. 4.1 is spurious, and is most likely due to a poor choice of initial guesses for the parameters in the fitting program. The corresponding line in Fig. 4.2 is suppressed due to its large size, which masked the behaviour of the other results in the graph.

Axial scans at two different values of plasma current, 1 A and 2 A, are shown in Fig. 4.5 to Fig. 4.8. The filament used was the same, so the values for position are directly comparable. The pressure was fixed at 2 mTorr, and the bias voltage was set at 96 V.

The hot temperature in Fig. 4.6 shows a slight plateau, with a value of approximately 25 eV, near the filament, which is not a very rigorous result due to interference between the probe and the system it is measuring. Beyond this region the temperature drops steadily and no meaningful distinction can be made between the two current values. The behaviour of the hot temperature with respect to position seems to be plasma current independent. The cold temperature shown in Fig. 4.5 behaves similarly; it declines from roughly 4 eV to 1 eV, and is not sensitive to the plasma current. Results above 90 cm can be ignored because the density becomes so low that the model fits a high temperature to this region.

The plot of the hot population's density with respect to probe position given in Fig. 4.8 does not show a clearly defined maximum in the case of the 2 A data. It is possible to say that the density reaches a maximum between 77 cm and 81 cm in both cases though. At greater distances, the hot density declines gradually. The fitted results for the 2 A data have a consistently higher density than the 1 A results.

The cold density plot, Fig. 4.7, shows a much more clearly defined maximum at 79 cm for the two choices of plasma current. There is strong evidence of a trough in the vicinity of the filament in this plot. The strong effect of increasing the plasma current on the cold density can be clearly seen here.

4.2 Pressure scans

4.2.1 Langmuir results

The pressure scan whose results are depicted in Fig. 4.9, Fig. 4.10, Fig. 4.11 and Fig. 4.12 was carried out under the following conditions: the bias voltage on the filament was set at 100 V, the filament current was 13.5 A throughout, the 30 mm magnets were positioned with their axis passing through the vessel centre, and the probe was positioned 2 cm from the vessel centre. Fig. 4.13 was performed with a base filament current of 14.22 A, a filament bias voltage of 60 V, using the 30 mm magnets to confine the plasma.

The cold density shown in Fig. 4.9,displays a rapid initial increase at low pressures and increases more slowly at higher pressures. The increase in the neutral density increases the cross section for collisions of the electrons from the filament, and therefore increases the cold density.

The hot density is largely unaffected by the increase in neutral density as shown by Fig. 4.13 and Fig. 4.9. The hot temperature falls gradually as the neutral density (pressure) increases. This may be due to a growing fraction of the electrons from the filament quickly losing at least some of their energy to collisions.

The results for the cold temperature in Fig. 4.10 and Fig. 4.13 are contradictory, since the temperature is largely constant in the former and rises slightly in the latter. The data was obtained in different experimental runs and the differences in the choices of initial guesses in the program may have played a role in creating a spurious outcome.

The floating potential, shown in Fig. 4.12, becomes more positive as the pressure is increased. It changes rapidly as the pressure increases from 0.7 mTorr to 1.0 mTorr and more gradually after that.

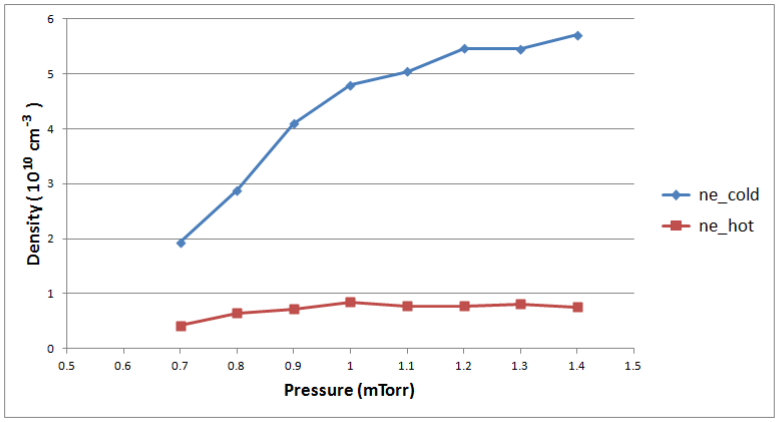

Fig. 4.9: The relationship between the pressure and the hot and cold densities at a filament bias voltage of 100V

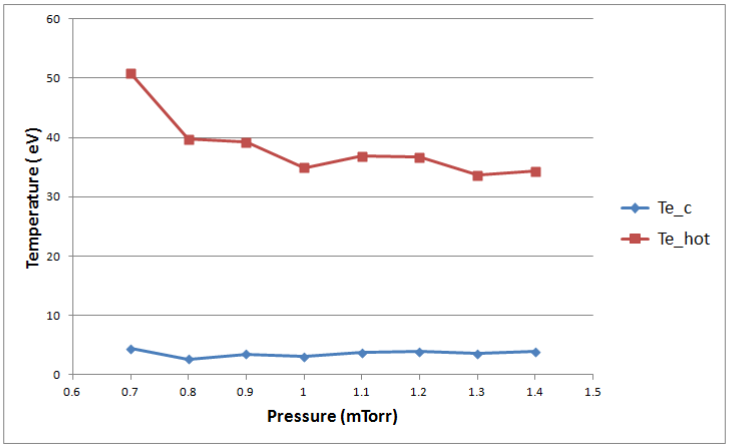

Fig. 4.10: The relationship between the pressure and the hot and cold temperatures at a filament bias voltage of 100V

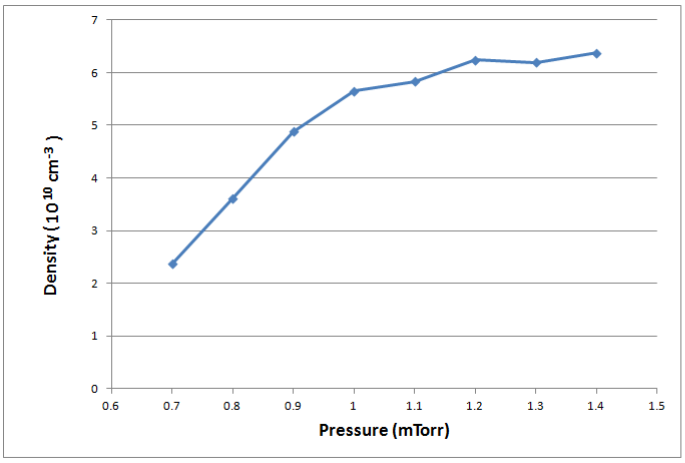

Fig. 4.11: The relationship between the pressure and the total density at a filament bias voltage of 100V

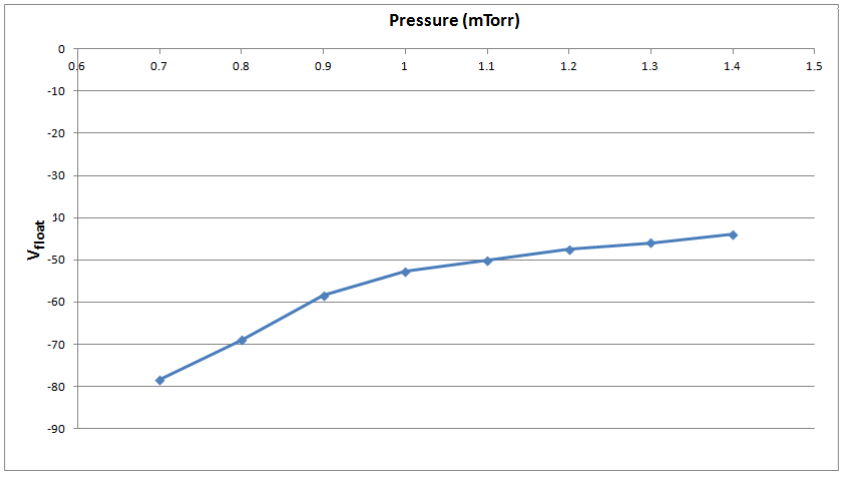

Fig. 4.12: The relationship between the pressure and the floating potential at a filament bias voltage of 100V

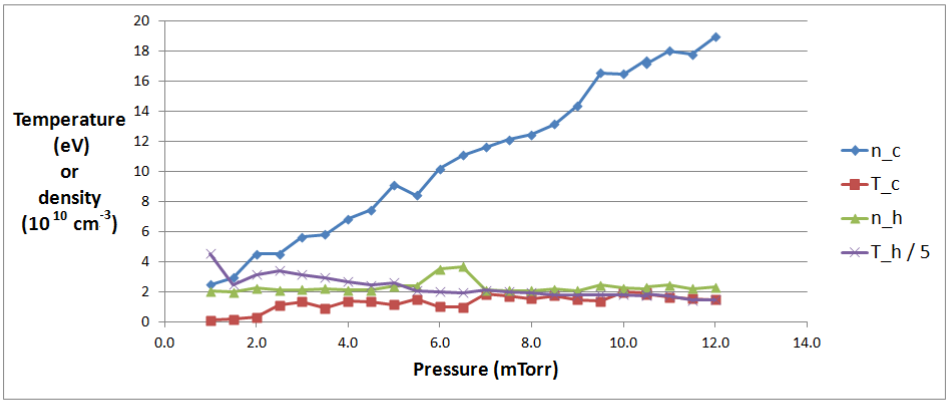

Fig. 4.13: Density and temperature with respect to pressure

4.2.2 Spectroscopic results

The results depicted in Fig. 4.14 and Fig. 4.15 result from a scan in pressure performed with a filament bias voltage of 60 V, confinement provided by the 30 mm magnets and a filament current of 14.22 A. In Fig. 4.15, the results have been divided by the plasma current to remove the increase in peak strength that is due to the increasing plasma current.

In Fig. 4.15, the ratio of the 667.8 nm line to that of the 706.5 nm line changes significantly with increasing pressure. This is clear evidence of a differing dependence on the neutral density.

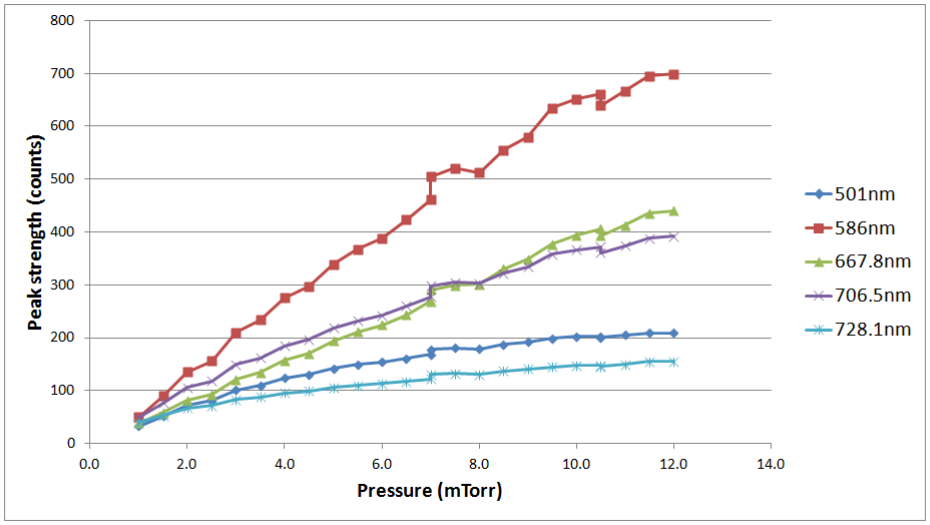

Fig. 4.14: A pressure scan at a filament bias voltage of 60V

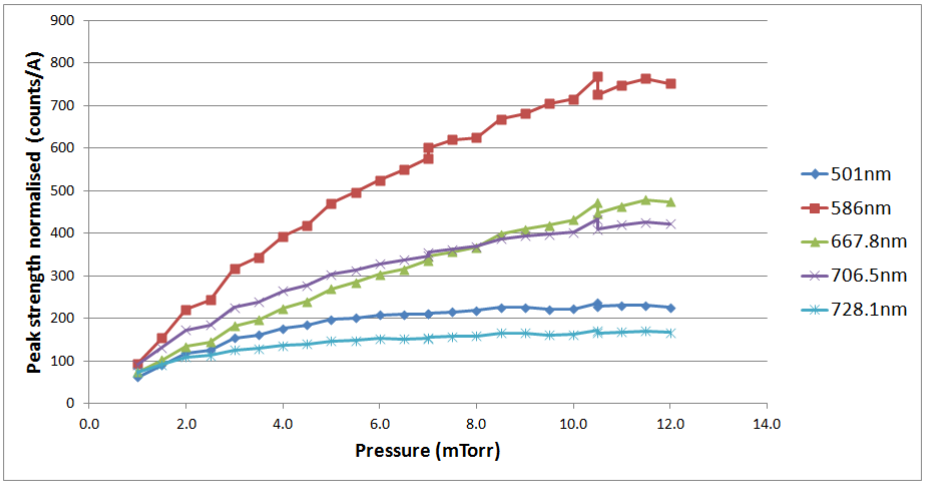

Fig. 4.15: A pressure scan at a filament bias voltage of 60V normalised to the plasma current

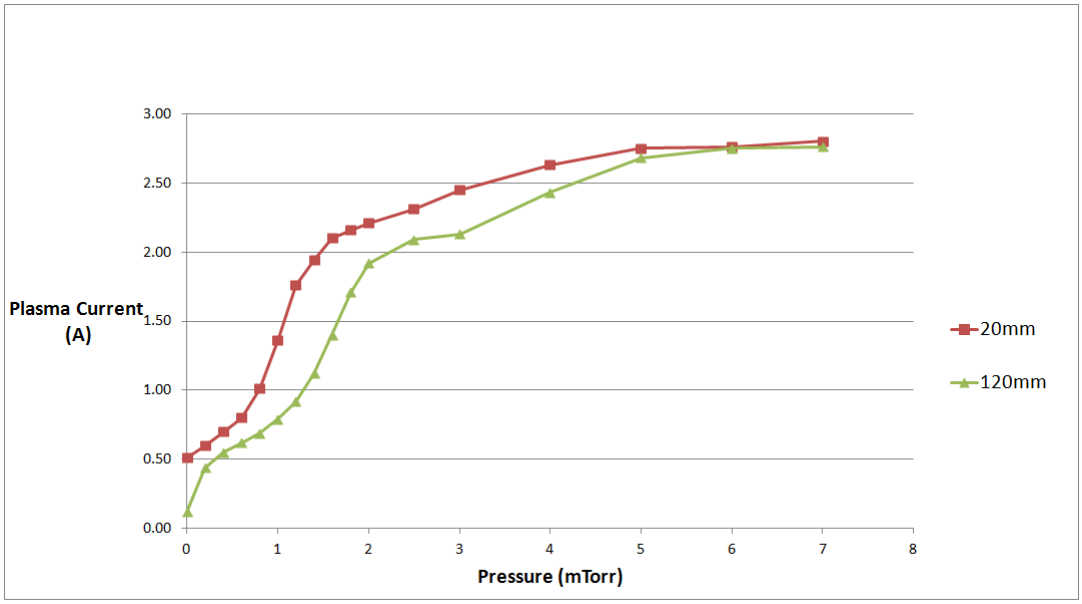

Fig. 4.16: A pressure scan at a filament bias voltage of 70V and filament current of 13.00A showing the effect of a varying pressure on the plasma current in an unmagnetised plasma at two values of throttle thickness

4.2.3 *Investigating relationship between pressure and plasma current*

The relationship between the pressure and the plasma current in an unmagnetised plasma is shown in Fig. 4.16. The apparatus was used in two different configurations - throttled (20mm) and unthrottled (120mm). A 20 mm throttled configuration meant that a 20 mm aluminium block was inserted to prevent the throttle from fully closing. Throttling reduces the strain on the pumps, but increases the release of unwanted gases from the vessel wall. Both configurations begin to converge on an identical value of plasma current as the pressure is increased. This is in line with expectations, since, even if there is outgassing in one configuration more than the other, this will be overwhelmed by the increasing pressure of helium.

The longer residency times in the throttled configuration may lead to an increase in the He* metastable population which could account for part of the increase in plasma current. This would require further investigation.

4.3 Plasma current scans

4.3.1 Langmuir results

Fig. 4.18 and Fig. 4.17 were acquired with the following configuration: the pressure was 1 mTorr, the filament bias voltage was 70 V and the confinement was provided by the 30 mm magnets.

The cold density, shown in blue in Fig. 4.18, was found to be directly proportional to the plasma current over this range of current values. The hot density begins to deviate from a straight line relationship as the plasma current increases, as can be seen by examining the red line in Fig. 4.18. The strong relationship between the plasma current and the density of secondary electrons is in line with the theoretical expectations outlined earlier in this thesis.

Both the hot and cold temperatures, shown in red and blue respectively in Fig. 4.17, increase slowly with increasing plasma current. The region of low plasma current in Fig.4.17 shows the greatest rate of change. For ease of comparison, this diagram also show the inverse of half the floating potential for ease of comparison. It is clear from the diagram that the floating potential and the hot temperature have the same functional dependence.

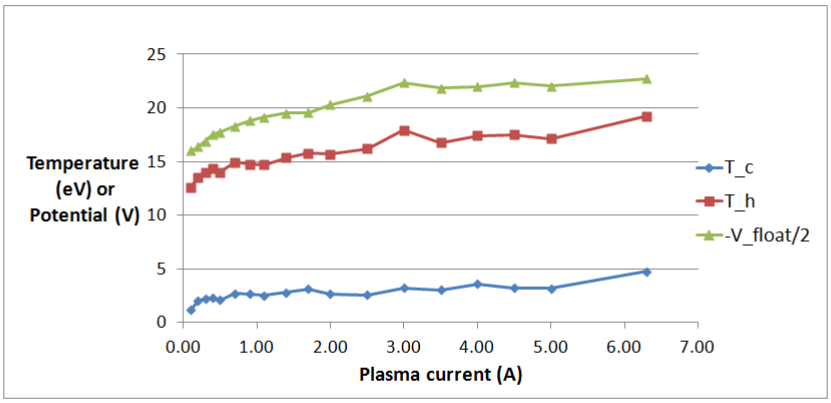

Fig. 4.17: The relationship between the plasma current, the hot and cold temperatures and the floating potential

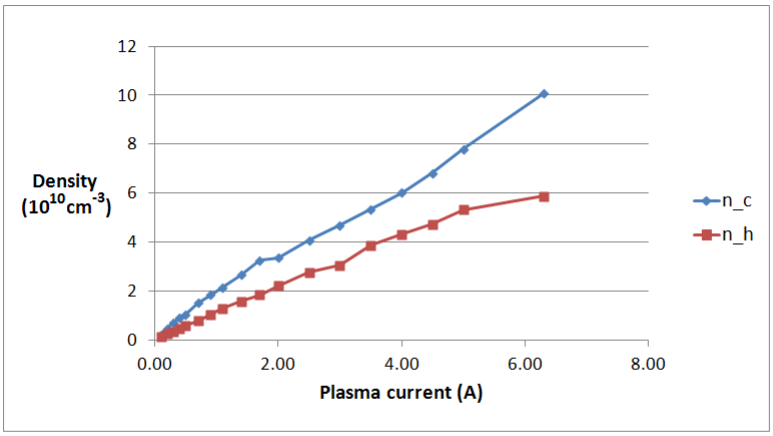

Fig. 4.18: The relationship between the plasma current and the hot and cold densities

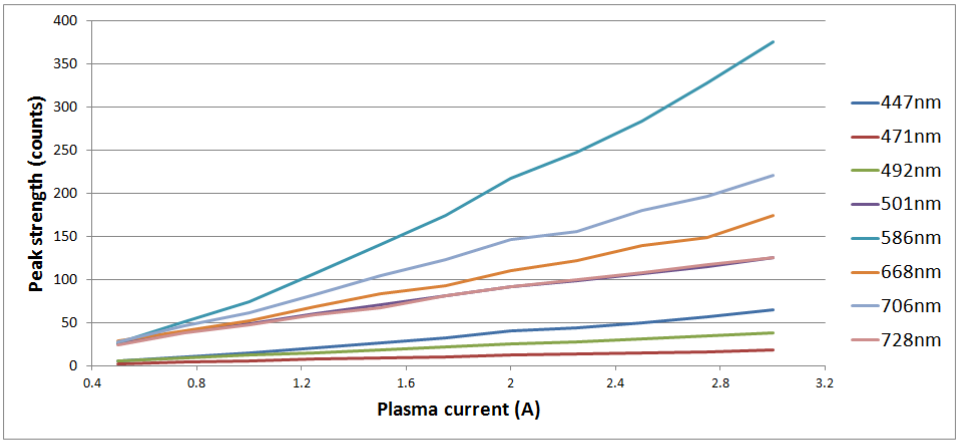

Fig. 4.19: Peak strengths plotted against plasma current for a pressure of 1 mTorr

4.3.2 Spectroscopic results

Fig. 4.19 plots line emission intensities as a function of plasma current. Experimental conditions were as follows: the pressure was set at 1 mTorr, the filament bias voltage was 70 V, and the confinement was provided by the 30mm magnets aligned with the centre of the vessel.

It shows that the emission line intensities increased linearly or super-linearly as the plasma current was increased. Combining the spectral results with the Langmuir probe results (Fig. 4.18 and Fig. 4.17) shows that the increase in density supplies the extra plasma current. This increasing density gives rise to the increase in the signal recorded by the spectroscope.

The data in Fig. 4.20 shows the effect of an increased plasma current on the peak strength estimated for the 728.1 nm line at several voltages. This data was obtained with the pressure set to 1 mTorr and the confinement provided by the 30 mm magnets. It shows an interesting result: the strength of a line increases with increasing voltage up to 100 V and diminishes again beyond this. It is possible that higher bias voltages make more states accessible to hot electrons and changing the collision cross section.

The ratios of the 667.8 nm ($3d^1D - 2p^1P$) line to the 728.1 nm ($3s^1S - 2p^1P$)

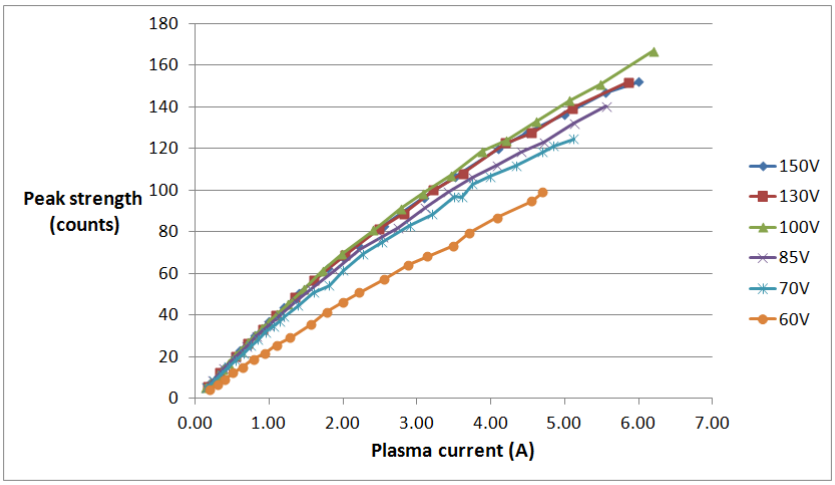

Fig. 4.20: Peak strengths of 728.1 nm line for several bias voltages as the plasma current in increased.

line, and the 728.1 nm line to the 706.5 nm ($3s^3S - 2p^3P$) line, are shown in Fig. 4.21. According to the papers by Andrew and O'Mullane[12]; and Field, Carolan, Conway and O'Mullane[13], the ratio 667.8/728.1 is density dependent, and the ratio of 728.1/706.5 is temperature dependent. It is shown [13] that, for three distinct choices of density ($10^{18}m^{-3}$,$10^{18}m^{-3}$ and $10^{18}m^{-3}$), the the temperature dependent emission line intensity ratio 728.1/706.5 increases by a factor of 100 as the temperature is increased from 10 eV to 1000 eV. Similary it is shown [13] that the density dependent emission line intensity ratio (667.8/728.1) increases by a factor of 10 when the density is increased from $10^{18}m^{-3}$ to $10^{20}m^{-3}$.

The results shown in Fig. 4.21, and later in Fig. 4.29, are in disagreement with this. The 728.1/706.5 ratio declines with increasing plasma current as shown, where plasma current is used as a measure for density. The decrease is more gradual beyond 1.5 A. The 667.8/728.1 ratio changes with plasma current but not in a steady manner.

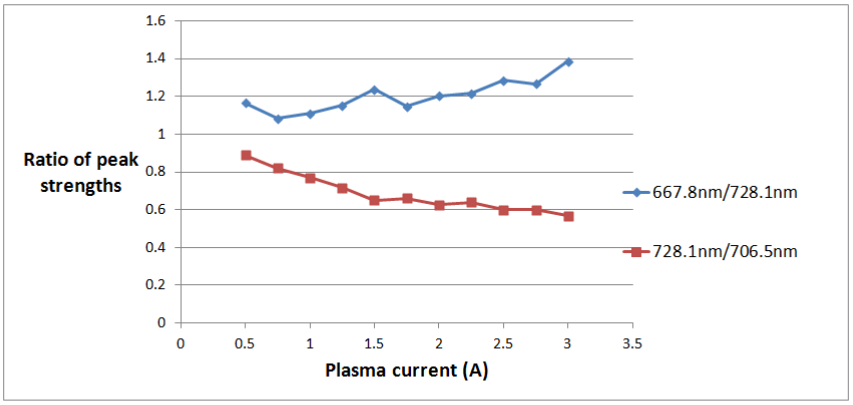

Fig. 4.21: Ratio of selected lines plotted against increasing plasma current

4.3.3 Investigating the relationship between plasma current and filament current

Fig. 4.22 shows a scan of the filament current needed to produce a given plasma current. The filament bias voltage was set at 70 V, the pressure at 1 mTorr and the 30 mm magnets were used to confine the plasma. The scan was performed in ascending and descending values of the plasma current. It is clear from the resulting plot that there exists no disparity between the two individual sections of this experiment; the conditions did not change as the experiment was performed. The plasma current seems to be roughly equal to the square root of the filament current.

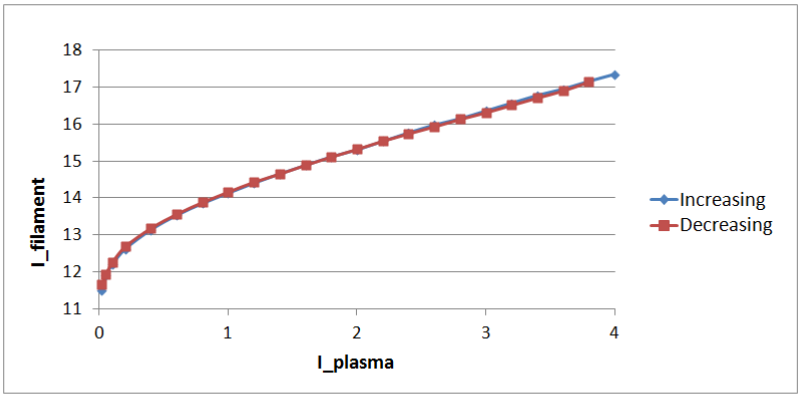

Fig. 4.22: A scan of the filament current needed to generate a given plasma current

4.4 Energy scans

The bias voltage, V_c, is the energy provided to the electrons to accelerate them away from the filament. Adjusting the bias voltage using the *Delta Elektronica SM 400- AR-8* allowed the energy of the primary electrons to be varied.

4.4.1 Langmuir results

The investigation into the effect of changing the bias voltage on the density and temperature was performed using the 50 mm magnets to provide confinement. The pressure was held at 1 mTorr and the probe was 3 cm from the filament.

Increasing the bias voltage should increase the energy of electrons leaving the filament. Hence the hot temperature would be expected to rise with the voltage. This is partially confirmed in Fig. 4.26; the hot temperature increases with the filament voltage from 65 V to 90 V, and thereafter it decreases slightly again. The reason for this decrease is not clear. It is possible that the values obtained for voltages around 90 V are slightly incorrect due to an inaccuracy with the pressure, which is the most difficult parameter to control, and was held at a low value during this experiment meaning that there was an even greater fractional error. If a straight line is fitted to the results for the hot temperature, it is clear that it has a positive slope.

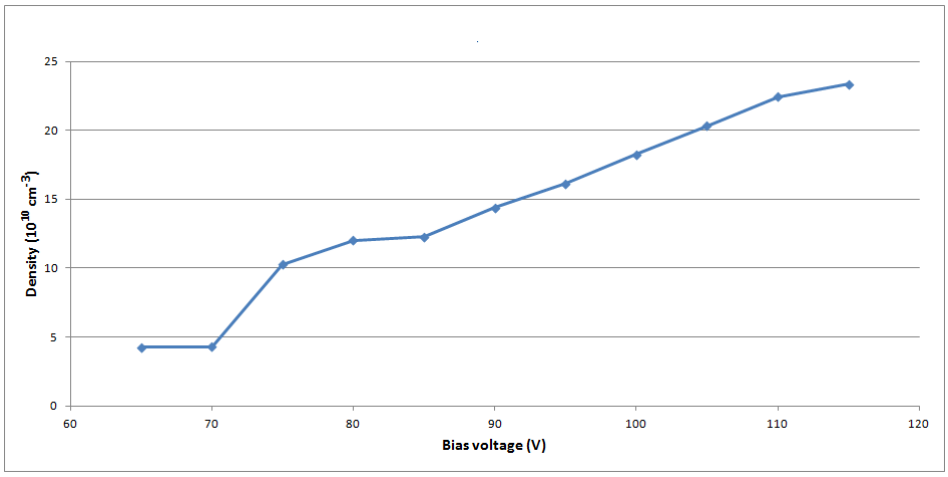

Fig. 4.23: The relationship between total density and bias voltage at 1 mTorr

The cold temperature in Fig. 4.26 shows no clear relationship with the bias voltage. It also has a slight increase around 90 V, which reinforces the conjecture that the peak in the hot temperature at this value is excessive.

The floating potential steadily increases with increasing bias voltage, as shown in Fig. 4.24.

The total density and cold density increase steadily with increasing voltage as shown in Fig. 4.23 and Fig. 4.25, respectively. The increasing energy of electrons from the filament would result in more accessible transitions in helium being accessed, and this would result in an increased cold density. The hot density shows a weaker increase with increasing voltage - it roughly doubles over the range of bias voltage.

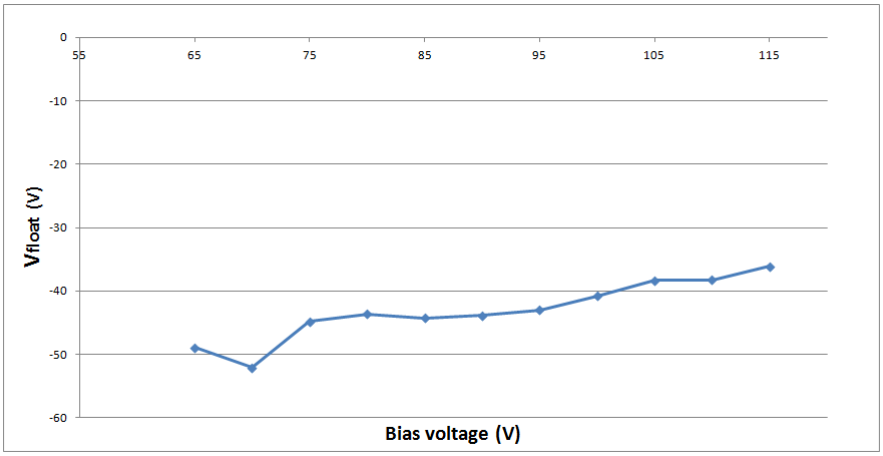

Fig. 4.24: The relationship between the floating potential and bias voltage at 1 mTorr

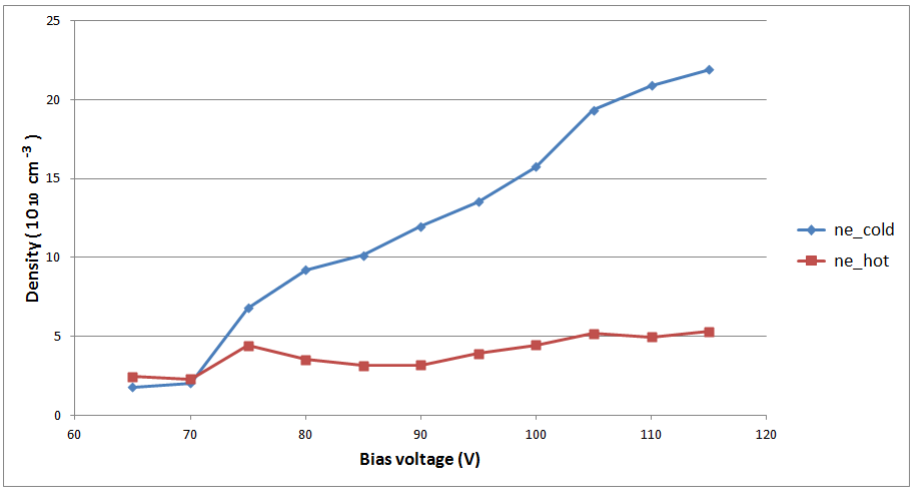

Fig. 4.25: The relationship between the bias voltage and the hot and cold densities at a pressure of 1 mTorr

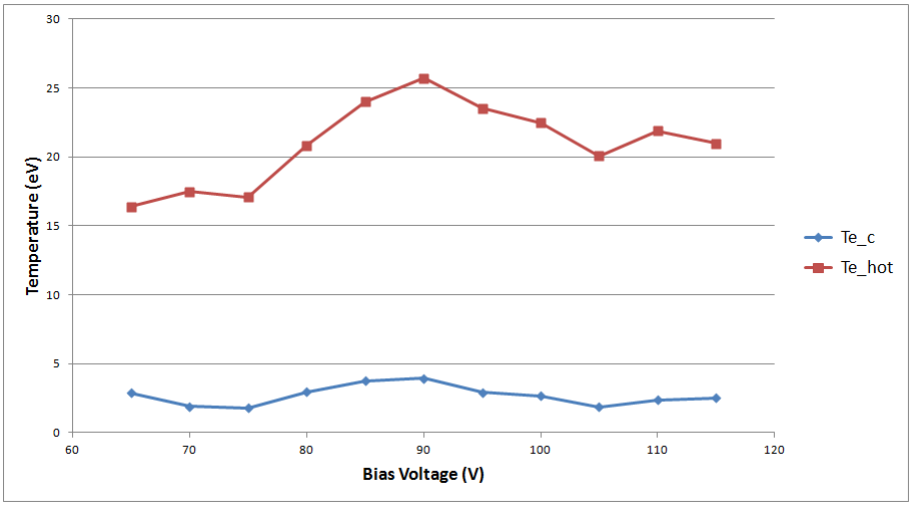

Fig. 4.26: The relationship between the bias voltage and the hot and cold temperatures at a pressure of 1 mTorr

4.4.2 Spectroscopic results

The results of a voltage scan which was carried out at a plasma current of 1.5 A is shown in Fig. 4.27. Fig. 4.28 shows the strength of the 728.1 nm line in several pressure regimes as the voltage was increased. The plasma current corresponding to this set was 2.0 A.

The results shown in Fig. 4.27 indicate a steady increase in the line strength as the bias voltage is increased. This is most prominent in the 586 nm and 667.8 nm lines.

The inversion of the order that occurs for the 0.7 mTorr and 0.9 mTorr values of the strength of the 728.1 nm line in Fig. 4.28is possibly due to errors in the measurement process. These were the lowest two pressures examined, and therefore had the greatest associated errors. All the lines show an initial rapid increase in strength with voltage before reaching a plateau. The higher pressure runs, e.g. 4.5 mTorr, take longer to reach this steady value. The magnitude of the peak strength increases with increasing pressure, which, if used with the information in the section on Langmuir results for pressure scans, serves to confirm that the cold population makes a significant contribution to the line strengths observed by the the spectroscope.

The results shown in Fig. 4.29 when viewed with those in Fig. 4.21 show the variation in the given ratios with respect to increasing bias voltage (temperature) and plasma

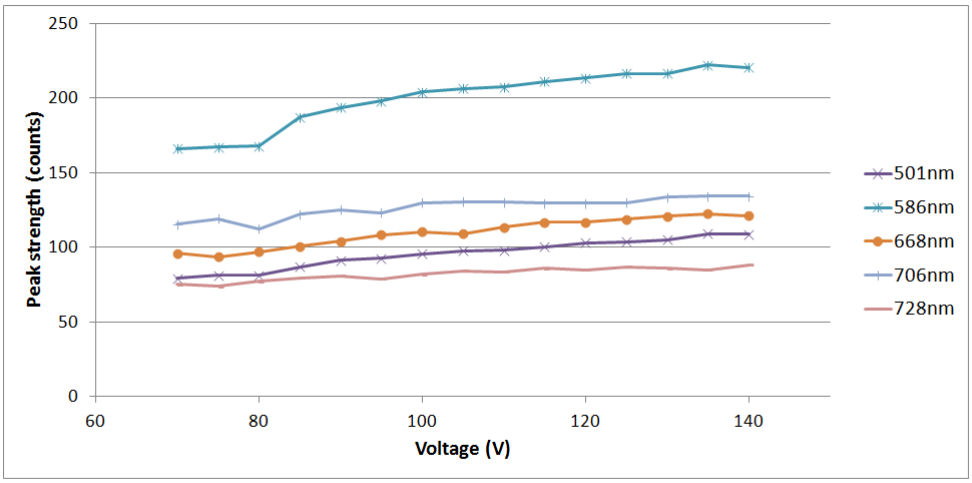

Fig. 4.27: Voltage scan at a pressure of 1 mTorr

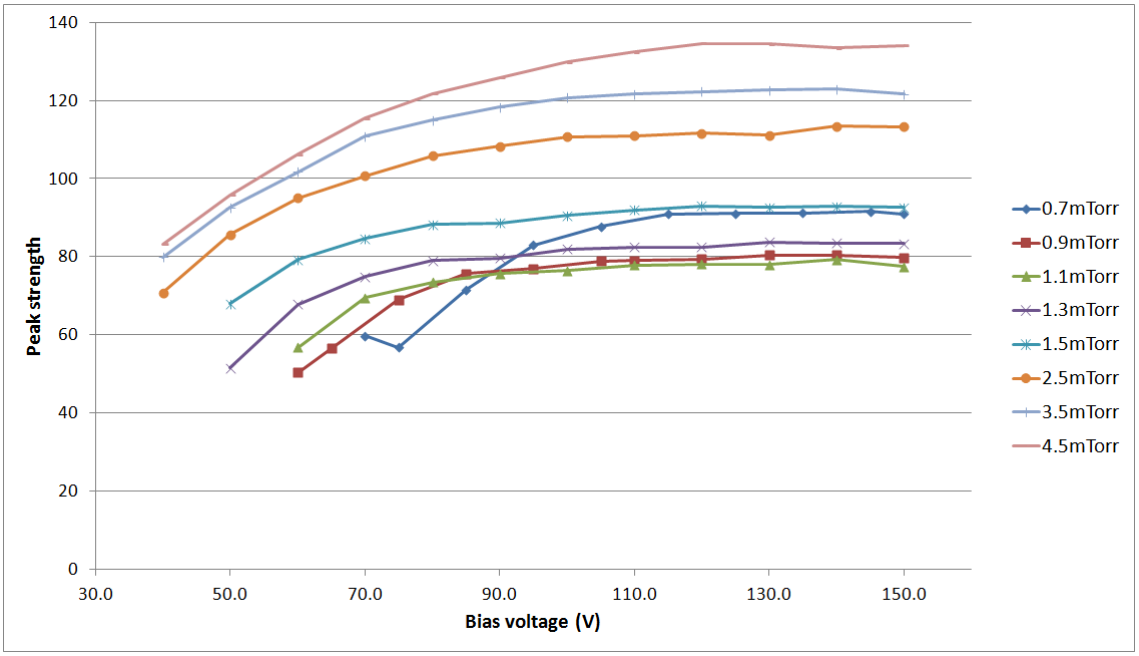

Fig. 4.28: Voltage scan at several pressures showing strength of 728.1 nm line

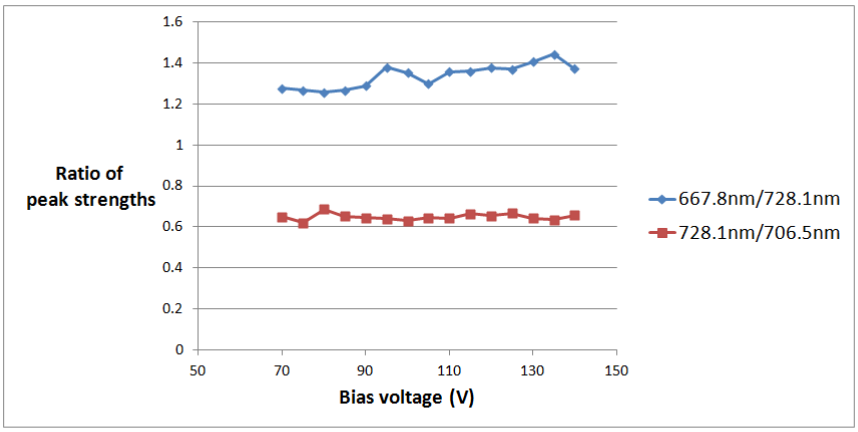

Fig. 4.29: Ratio of selected lines plotted against bias voltage

current (density) respectively. The results for the 728.1/706.5 ratio are dramatically different to the predictions from previous works[12]. The $728.1nm/706.5nm$ ratio was found to be independent of increasing voltage in this work which contradicts the expectation that this ratio would be temperature dependent.

The reason for the discrepancy between this work and previous works may be that the cold population contributes most to signal recorded by the spectroscope and that while the hot temperature is increased by increasing the bias voltage, the cold temperature does not significantly change whereas the cold density does (see Fig. 4.25 and Fig. 4.26)

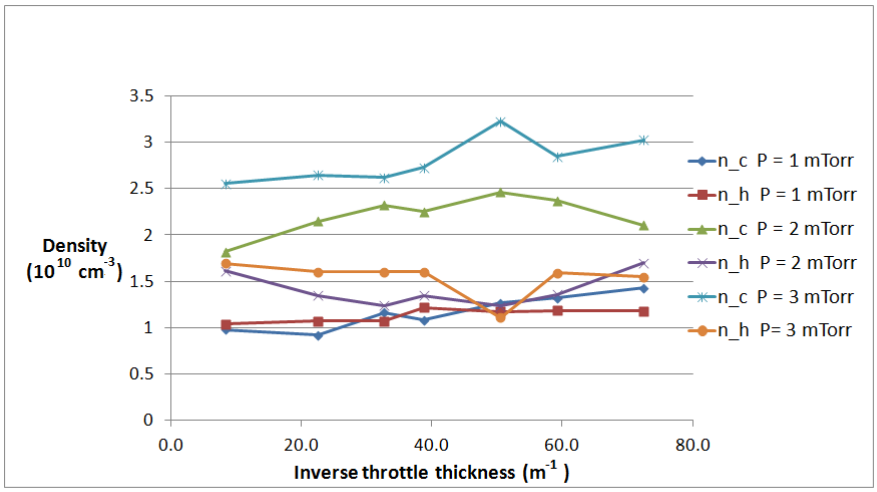

Fig. 4.30: Hot and cold densities plotted against inverse of throttle thickness

4.5 Investigating impact of the throttle thickness on fitted temperatures and densities

An investigation was performed into the influence of the throttle thickness on the hot and cold densities at 3 different pressures: 1 mTorr, 2 mTorr and 3 mTorr . The voltage was held at 70 V and the plasma current was fixed at 1.0 A. The results are shown in Fig. 4.30. They show that as pressure is increased, the difference between the cold and hot densities increases. They show no clear trend with hot densities, but for the cold densities, they show a slight increase as the inverse of the throttle width increases, i.e. as the throttle width becomes progressively thinner. The trend is most visible in the case where the pressure is 1 mTorr.

4.6 An investigation into changes in heating current

It was noticed that the creation of a plasma let to a significant change in the measured filament current, I_F. The nature of this relationship was investigated by creating a plasma at a given pressure and bias voltage, and then quenching the plasma using a sudden change in bias voltage. This was performed at two different values of pressure, 5 mTorr and 1 mTorr, and two different bias voltages, 50 and 70 V. The four sets of data

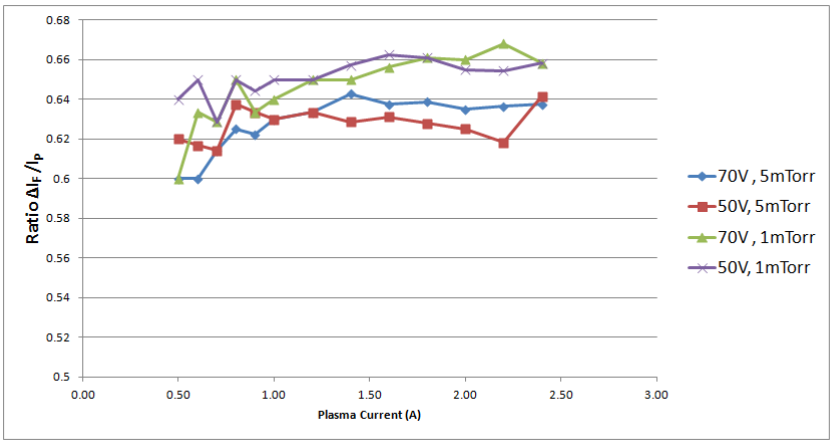

Fig. 4.31: Ratio of difference in filament current to the resulting plasma current

are plotted in Fig. 4.31. The ratio of the change in the filament current to the plasma current is seen to be largely independent of pressure and bias voltage for this choice of parameters. The ratio also fails to show a variation with increases in the plasma current I_{plas}.

It is plausible that the creation of a plasma produces another path within the circuit through which current can flow. The resistance of this path will depend on the geometry of the filament, and the variation of resistance along its length. This ratio may provide a measure of the lifespan of the filament, since, as the filament ages, it will narrow at points where it is weakening.

The change in voltage across the heating circuit depicted in Fig. 4.32 can be expressed as follows (work by P McCarthy):

$$V_{fil} = I_{fil}(R_{fil})a + (I_{fil} - I_{plas})(1-a)R_{fil}. \tag{4.6.1}$$

Similarly, the change in voltage across the plasma circuit is given by:

$$V_{disch} = I_{plas}R_{plas} + (I_{plas} - I_{fil})(1-a)R_{fil}. \tag{4.6.2}$$

Where V_{disch} refers to the discharge voltage, I_{fil} refers to the filament current, I_{plas} refers to the plasma current, $1-a$ is the fraction found experimentally, i.e. roughly 0.6.

Rearranging Eqn. 4.6.1 to isolate I_{fil} gives:

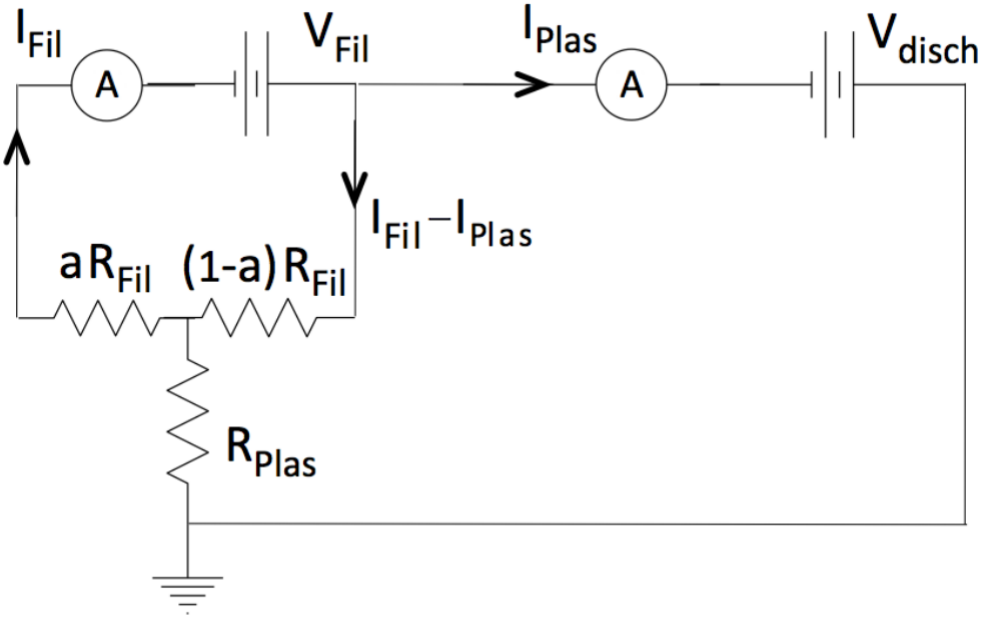

Fig. 4.32: Circuit diagram of plasma and filament circuit

$$I_{fil} = \frac{V_{fil}}{R_{fil}} + (1-a)I_{plas}. \tag{4.6.3}$$

The first term in Eqn. 4.6.3 can be identified as the base filament current in the absence of a plasma. The second term is the $0.6I_{plas}$ found experimentally.

Similarly, by rearranging Eqn. 4.6.2 in terms of I_{plas}, the following equation is obtained:

$$I_{plas} = \frac{V_{disch} + (1-a)V_{fil}}{R_{plas} + a(1-a)R_{fil}}. \tag{4.6.4}$$

The numerator in Eqn. 4.6.4 is, as expected, the voltage across the plasma circuit. The denominator is given by the sum of the resistance of the plasma and a fraction of the resistance of the filament. Since $R_{fil} \approx 2\Omega$, and $R_{plas} \approx 35\Omega$, the second term represents a relatively small fraction of the first.

4.7 Investigating the magnetic confinement

The effect of withdrawing the 12 mm magnets from the wall of the vessel on the hot and cold densities is shown in Fig. 4.33. The data was obtained with the pressure set at 0.5 mTorr, the heating current at 14.00 A, the Langmuir probe was 3.5cm from filament centre. Two values of voltage were chosen, 45 V and 70 V.

The fall off in the cold density is most dramatic when the voltage is higher, the value halves when the magnets are moved 10 mm back from the walls. The falloff of the hot population when the bias voltage is 70V is also more rapid than that of the 45 V case. This implies that the lower voltages, and hence lower energy electrons, are more easily confined than the high energy ones, which is in line with expectations.

Fig. 4.34 and Fig. 4.35 show the behaviour of the densities and temperatures respectively, as the columns of magnets are increased in length from 0 magnets to their full length 29 individual magnets. The magnets used were once again the 12 mm magnets. The bias voltage was fixed at 70 V, the pressure at 3.0 mTorr, and the filament current was 14.00 A. The cold density when 3 magnets were in place was 1/49th of the cold density when the full stack is present, while the hot density increases by a factor of 20 over the same range. This demonstrates the dramatic effect of the presence of a magnetic mirror on the densities.

The hot temperature shows a slight increase over the range from 7 magnets to 29 magnets, but the cold temperature remains largely constant over the same range.

The influence of the magnetic field on the cold density at several values of pressure is depicted in Fig. 4.36. All four magnet diameters were utilised in this experiment. The bias voltage was held at 70 V, and the filament voltage was set at 14.00 A. As the pressure was increased from 1 mTorr to 9 mTorr. the cold densities increased dramatically in all cases but the 50mm magnets produced twice the cold density that the 12 mm magnets were able to maintain. The inversion of the expected order for the 23 mm and 30 mm magnets was possibly caused by an error in the recording of the pressure during the experiment.

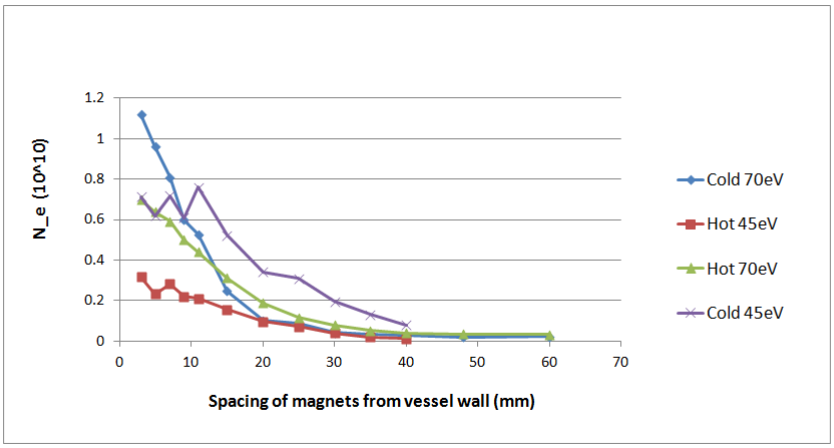

Fig. 4.33: Hot and cold densities at two bias voltages as magnet/wall separation is increased

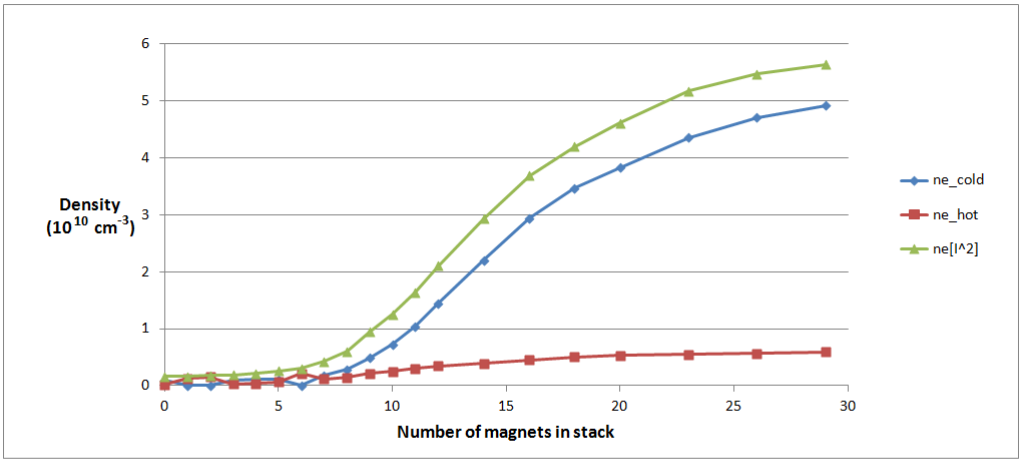

Fig. 4.34: Hot, cold and total densities as stack length is increased

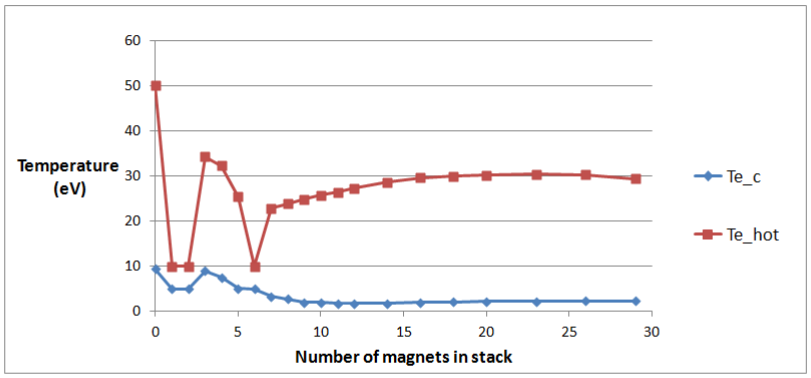

Fig. 4.35: Hot and cold temperatures as stack length is increased

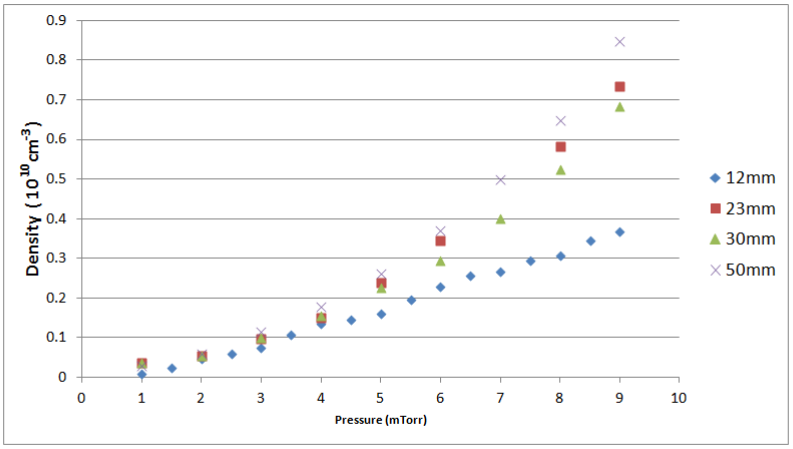

Fig. 4.36: Cold density plotted against pressure for all magnet diameters

5. CONCLUSION

Data collected at regular intervals along the axis of the cylindrical vessel showed, when analysed, that a doubling of the plasma current does not effect the magnitude of the hot or cold temperature at a given point. The changes in plasma current were shown to be related to an increase in the fitted values for the hot and cold densities. The fitted results from the analysis of this data displayed a clear area of reduced density near the filament centre, possibly due to beam effects.

Axial scans at several different pressures showed that higher hot electron temperatures were attained with the lowest pressure. Plots of the fitted values for the hot and cold densities showed a more sharply defined peak in the cold density profiles - the peak was symmetrically located with respect to the centre of the magnetic mirror and filament, suggesting that ring currents may play a role in this configuration.

The density of the cold electron population was shown to increase linearly with increasing bias voltage. The cold temperature was shown to be independent of increasing bias voltage.

Pressure scans at fixed bias voltage showed that the cold temperature is independent of the pressure, but that the hot temperature decreases with increasing pressure. The hot density was shown to be largely constant with respect to pressure, whereas the cold density increased steadily.

At high pressures it was convincingly demonstrated that differences in throttle thickness vanished. The thickness of the throttle led to significant changes in the resulting plasma current at low pressures.

It was shown in that there is a correlation between the temperature of the hot electron population and the floating potential, V_f, as the plasma current was varied.

The investigation into the ratio of line strengths obtained using the spectroscope

yielded results which conflicted with previously published work[12]. The 728.1 nm/706.5 nm ratio, which was previously shown to be temperature dependent, here showed a marked decrease with increasing plasma current (density), and was insensitive to increasing bias voltage (temperature). The 667.8 nm/728.1 nm ratio showed a slight increase with both increasing plasma current and bias voltage.

6. IDEAS FOR FUTURE RESEARCH

The area of low density near the filament found in the density profiles in scans of axial distance warrants further study. Examining this region as the pressure is changed would help establish if it is purely due to beam effects, because these would reduce in significance as the pressure is increased.

It would be interesting to perform an axial scan at several values of the bias voltage to give a more complete knowledge of the behaviour of the hot and cold densities and temperatures as the probe is retracted.

The ratio of the change in filament current on creation of a plasma to the resulting plasma current could be investigated further. The choices of pressure in the initial experiment - 1 mTorr and 5 mTorr - were distinct enough to say that the behaviour of the ratio was largely independent of the pressure, but the two values of voltage chosen -50 V and 70 V - were insufficient to allow such a conclusion to be drawn about the bias voltage with as much confidence.

By carrying out an error analysis on the method used for calculating peak strengths to generate the spectral results in this thesis it would be possible to investigate the weaker lines more thoroughly and examine their behaviour as the pressure, bias voltage and plasma current are adjusted.

More thorough pressure scans could be performed with the spectroscope. It would be interesting to see the behaviour of line strengths at several different values of bias voltage and separately of plasma current. It would also be interesting to expand on the result shown in Fig. 4.20, exploring the changing line strengths as the voltage is varied in the vicinity of 100 V.

The ratios of the weaker lines in the helium spectrum to each other could be studied in different regimes of pressure, bias voltage and plasma current to determine if any of

them are useful measures of density or temperature of electrons in the plasma.

If a more sensitive pressure gauge were employed it would be possible to investigate low pressure plasmas while increasing confidence in the validity of the output.

BIBLIOGRAPHY

[1] Francis F. Chen. *Introduction to Plasma Physics and Controlled Fusion, Volume 1: Plasma Physics*, 2nd edition, Plenum Press.

[2] R. O. Dendy.(editor) *Plasma Physics: an Introductory Course*, Cambridge University Press.

[3] Paul M. Bellan. *Fundamentals of Plasma Physics*, Cambridge University Press.

[4] T.J.M. Boyd and J.J. Sanderson. *The Physics of Plasmas*, Cambridge University Press.

[5] R. J. Goldston and P. H. Rutherford. *Introduction to Plasma Physics* , IOP Publishing.

[6] Z. Sternovsky, S. Robertson and M. Lampe,*Ion collection by cylindrical probes in weakly collisional plasmas: Theory and experiment* Phys. Plas. 10 (2003) 300.

[7] H. M. Mott-Smith and I. Langmuir. *The theory of collectors in gaseous discharges* Phys.Rev. 28 (1926) 727.

[8] I. H. Hutchinson *Principles of Plasma Diagnostics* Cambridge University Press

[9] Geoffrey V. Marr. *Plasma Spectroscopy*,Elsevier Publishing.

[10] P.J. Mc Carthy, B. Cahill, T.J. Morgan and R.A. Armstrong. *Comparison of probe and spectroscopic data in a* $Te > 10$ eV *magnetic mirror laboratory plasma.* 30th ICPIG, August 28th - September 2nd, 2011, Belfast, UK

[11] J.D. Swift and M.J.R. Schwar *Electrical Probes for plasma Diagnostics* Iliffe Books

[12] Y. Andrew and M. G. O'Mullane. *Sensitivity of calculated neutral helium line intensities and their ratios to uncertainties in excitation rate coefficients* Plasma Phys. Control. Fusion 42 (2000) 301307.

[13] A. R. Field, P. G. Carolan, N.J. Conway and M. G. O'Mullane. *Optimized instrumentation for edge T_e and n_e measurements on COMPASS-D tokamak from He I line intensity ratios* Review of Scientific Instruments 70 (1999) 355-358.

7. APPENDIX

7.1 Program to analyze spectral data

```
start = 2;
end = 20;
skip = 1;

(*{311,285,302,319,340},*)(*{1344,1320,1340,1355,1370},*)
Peaks = {{378, 360, 374, 384, 399},
   {495, 470, 485, 500, 510}, {525, 505, 515, 530, 545},
   {552, 538, 545, 557, 564}, {571, 558, 563, 583, 589},
   {592, 583, 588, 598, 603}, {609, 598, 602, 618, 623},
   {635, 618, 633, 650, 668}, {710, 700, 707, 718, 723},
   {734, 718, 723, 745, 765}, {802, 770, 790, 815, 835},
   {862, 840, 855, 872, 886}, {889, 874, 884, 908, 918},
   {1135, 1110, 1130, 1155, 1170},
   {1379, 1355, 1370, 1425, 1450}, {1505, 1470, 1490, 1520, 1545},
   {1565, 1540, 1560, 1580, 1600}};
dim = Dimensions[Peaks][[1]];
fin = Table[0, {ix, 1, end}, {m, 1, dim}];

Corr = {(*1,*)1, 2.34149, 2.05876, 1.75354, 1.62368, 1.5089, 1.39391,
   1.31752,
   1.18508, 1.13375, 1.05463, 0.81588, 0.830039, 1.34274,(*2.208822,*)
   2.40215,
```

```
    3.81238, 4.84813};

Clear[data]
SetDirectory[
  "C:\Users\Brendan\Documents\Main\MSc\Research Daily Record\Week \
10\Friday\data"];
prestr = "spectrum";
 trailstr = ".txt";

Off[General::stop, General::spell, General::spell1, Graphics::gptn,
 Min::nord,
  Max::nord, LessEqual::nord, ReplaceAll::reps, Power::infy,
 FindFit::lstol,
  Plot::plnr, General::ovfl, General::unfl, FindFit::njnum,
  SingularValueDecomposition::mindet, GridLines::grid, Set::partw,
 Divide::infy, ReadList::nffil]

nfiles = 200;
nres = 2 nfiles;
ccodes = Table[0, {i, nfiles}];
 faar = ccodes;

Do[ccodes[[i]] = {48, 48, 48 + i}, {i, 1, 9}];
Do[ccodes[[i]] = {48, 48 + Floor[i/10], 48 + Mod[i, 10]}, {i, 10,
    Min[99, nfiles]}];
If[nfiles > 99,
 Do[ccodes[[i]] = {48 + Floor[i/100], 48 + Mod[Floor[i/10], 10],
     48 + Mod[i, 10]}, {i, 100, nfiles}];]
```

```
Do[faar[[i]] =
    prestr <> FromCharacterCode[ccodes[[i]]] <> trailstr, {i, 1,
    nfiles}];

mydir = Directory[];
slash = "\\";
Print[" First filename in sequence= ", mydir, slash, faar[[01]]];
neresa = Table[0, {i, nres}];

(*failed = 0;*)

Do[{

    taname = faar[[ix]];

    data = ReadList[taname, Word, WordSeparators -> {" ", "\t"}];
    Print[" Filename is: ", mydir, slash, taname];
    datlength = Length[data];

    (*If[datlength==0,failed = failed+1,failed = failed];*)
    If[datlength == 0,
      Print["File is blank: ", mydir, slash, faar[[ix]]]]
     If[datlength == 0, ix += 1, ix = ix];
    If[datlength == 0, Continue[]];




    init = Take[data, {33, 33}];
```

```
StringToNumber[s_String] :=
 Block[{ss, result}, ss = StringToStream[s];
  result = Read[ss, Number]; Close[ss]; result];
integtime = Map[StringToNumber, init, {1}];



ingtim = integtime[[1]]/1000;
(*it=ingtim/1000;*)



Print[" Integration time is = ", ingtim    "ms" ];

Print[" Number of data points  is = ", Length[data]    ];
data[[76]];
DStart = 76;
DEnd = 4171;

adat = Take[data, {DStart, DEnd}];
amt = Partition[adat, 2];
StringToNumber[s_String] :=
 Block[{ss, result}, ss = StringToStream[s];
  result = Read[ss, Number]; Close[ss]; result];
aplot = Map[StringToNumber, amt, {2}];
grrr = aplot;
tr = Transpose[aplot];

wave = tr[[1]];
Print[" Number of wavelenth data points  = ", Length[wave]]
```

```
 ClearAll[inten];
inten = tr[[2]];
Print[" Number of Intensity data points = ", Length[inten]]
 Do[



    Lpeak = Peaks[[m, 1]];
  LpreStr = Peaks[[m, 2]];
  LpreEnd = Peaks[[m, 3]];
  LpstStr = Peaks[[m, 4]];
  LpstEnd = Peaks[[m, 5]];



  (*Print["Peak at = ",aplot[[Lpeak,1]]"nm"  ]*)
  aplot[[LpreStr]];
                    aplot[[LpreEnd]];
  aplot[[LpstStr]];
  aplot[[LpstEnd]];

  pre = Take[aplot, {LpreStr, LpreEnd}];
  post = Take[aplot, {LpstStr, LpstEnd}];
  L = Join[pre, post];

  f[x_] = Fit[L, {1, x}, x];

  pkuc = Take[aplot, {LpreEnd + 1, LpstStr - 1}];
  pkuctr = Transpose[pkuc];
  lamuc = pkuctr[[1]];
  intc = f[lamuc];
```

```
tor = Transpose[aplot];


wavev = tor[[1]];
Length[wavev];
Intenv = tor[[2]];
wavev;
Intenv;


res = Length[Intenv] - LpreEnd;


d = Drop[Intenv, LpstStr - 1];
g = Drop[Intenv, -res];
Length[Intenv];
intc;
d;
g;
Length[intc];
Length[d];
Length[g];
a = Join[g, intc, d];


b = Join[wavev, a];
Length[b];
u = Partition[b, 2048];
Clear[aplot];
aplot = Transpose[u];
```

```
    transform = Transpose[aplot];
    intennew = transform[[2]];

    intpeaks = inten - intennew;
    er = Join[wave, intpeaks];
    pks = Partition[er, 2048];
    Parpeaks = Transpose[pks];



    ttl =
     Table[Total[
       Table[intpeaks[[Peaks[[i, 3]] + j]]/ingtim, {j,
         Peaks[[i, 4]] - Peaks[[i, 3]]}]], {i,
       Dimensions[Peaks][[1]]}];
    corttl = Table[ttl[[i]]*Corr[[i]], {i, Dimensions[Corr][[1]]}];

    fin[[ix]] = corttl;



    , {m, 1, dim}]



  }, {ix, start, end, skip}];

pk = Table[wave[[Peaks[[m, 1]]]], {m, 1, dim}];
laba = Join[{Index}, pk];
```

```
fint = Table[Join[{m}, fin[[m]]], {m, start, end}];
flp = Join[{laba}, fint];

Export["Output.xls", flp, "XLS"]
```